

# Photospheric Velocity Gradients and Ejecta Masses of Hydrogen-poor Superluminous Supernovae: Proxies for Distinguishing between Fast and Slow Events

Réka Könyves-Tóth and József Vinkó 1,2,3 to 1 Konkoly Observatory, CSFK, Konkoly-Thege M. ut 15-17, Budapest, 1121, Hungary; konyvestoth.reka@csfk.mta.hu Department of Optics & Quantum Electronics, University of Szeged, Dóm tér 9, Szeged, 6720, Hungary ELTE Eötvös Loránd University, Institute of Physics, Pázmany Péter sétány 1/A 1117, Budapest, Hungary Received 2020 November 2; revised 2020 December 8; accepted 2020 December 22; published 2021 March 2

#### Abstract

We present a study of 28 Type I superluminous supernovae (SLSNe) in the context of the ejecta mass and photospheric velocity. We combine photometry and spectroscopy to infer ejecta masses via the formalism of radiation diffusion equations. We present an improved method to determine the photospheric velocity by combining spectrum modeling and cross-correlation techniques. We find that Type I SLSNe can be divided into two groups according to their pre-maximum spectra. Members of the first group have a W-shaped absorption trough in their pre-maximum spectrum, usually identified as due to O II. This feature is absent in the spectra of supernovae in the second group, whose spectra are similar to that of SN 2015bn. We confirm that the pre- or near-maximum photospheric velocities correlate with the velocity gradients: faster evolving SLSNe have larger photospheric velocities around maximum. We classify the studied SLSNe into the Fast or the Slow evolving group according to their estimated photospheric velocities, and find that all those objects that resemble SN 2015bn belong to the Slow evolving class, while SLSNe showing the W-like absorption are represented in both Fast and Slow evolving groups. We estimate the ejecta masses of all objects in our sample, and obtain values in the range 2.9  $(\pm 0.8)$ –208  $(\pm 61) M_{\odot}$ , with a mean of 43  $(\pm 12) M_{\odot}$ . We conclude that Slow evolving SLSNe tend to have higher ejecta masses compared to the Fast SLSNe. Our ejecta mass calculations suggests that SLSNe are caused by energetic explosions of very massive stars, irrespective of the powering mechanism of the light curve.

Unified Astronomy Thesaurus concepts: Supernovae (1668); Ejecta (453); Radiative transfer (1335)

#### 1. Introduction

A new class of transients, the so-called superluminous supernovae (SLSNe), was discovered and extensively studied over the past two decades. These extremely luminous events have at least  $\sim 10^{51}$  erg total radiated energy, leading to an absolute brightness of M < -21 in all optical wavelength bands (Quimby et al. 2011; Gal-Yam 2012, 2019a). It has also been reported that these supernovae (SNe) prefer to explode in dwarf galaxies having low metallicity and high specific star formation rate (Chen et al. 2013, 2017c; Lunnan et al. 2013, 2014; Leloudas et al. 2015; Angus et al. 2016; Japelj et al. 2016; Perley et al. 2016; Hatsukade et al. 2018; Schulze et al. 2018), although some counterexamples are also known. For example, PTF10tpz (Arabsalmani et al. 2019), PTF10uhf (Perley et al. 2016), and SN 2017egm (Chen et al. 2017b; Nicholl et al. 2017b; Bose et al. 2018; Izzo et al. 2018; Yan et al. 2018; Hatsukade et al. 2020) occurred in relatively bright and metalrich, or, at least not metal-poor, host galaxies. The recent publications of De Cia et al. (2018), Lunnan et al. (2018), and Angus et al. (2019) revealed that this population is quite multitudinous: some lower-luminosity transients (e.g. DES14C1rhg with  $M_r = -19.4$ ; Angus et al. 2019) have also been classified as SLSNe, because of the similar photometric or spectroscopic evolution to known, well-observed SLSNe (e.g., Quimby et al. 2018; Inserra 2019).

Similarly to the traditional/normal SNe, SLSNe can also be separated into two main subclasses: the H-poor Type I (SLSNe-I), and the H-rich Type II SLSN group (Branch & Wheeler 2017). The latter are divided into two distinct populations: the luminosity of Type IIn SLSNe is powered by the strong interaction with the surrounding, massive

circumstellar medium (CSM; e.g. SN 2006gy; Smith et al. 2007 or CSS121015; Benetti et al. 2014), and have similar spectroscopic properties and evolution to normal Type IIn SNe (Branch & Wheeler 2017). The representatives of the second group, called Type II SLSNe, show no visible signs of CSM interaction (e.g., SN 2013hx and PS15br; Inserra et al. 2018).

This study focuses on several events belonging to the H-poor SLSN class. The members of SLSNe-I are usually revealed to be spectroscopically similar to normal Ic or BL-Ic SNe (e.g., Pastorello et al. 2010b), with the difference that events in the former class have larger luminosities. SLSNe-I can be also separated into two groups (Inserra et al. 2018): the Fast (e.g., SN 2005ap; Quimby et al. 2007, SN 2010gx; Pastorello et al. 2010b, SN 2011ke; Inserra et al. 2013) and the Slow evolving events (e.g., SN 2010kd; Könyves-Tóth et al. 2020; Kumar et al. 2020, PTF12dam; Nicholl et al. 2013, SN 2015bn; Nicholl et al. 2016b), with an average light-curve (LC) rise time of  $\sim$ 28 days and  $\sim$ 52 days, respectively. Inserra et al. (2018) examined a sample of SLSNe statistically, and showed that Slow evolving SLSNe exhibit lower, and slowly evolving, or nearly constant photospheric velocities ( $v \leq 1$  $12,000 \text{ km s}^{-1}$ ) from the maximum to +30 days phase, compared to the Fast evolving events having  $v \ge 12,000 \,\mathrm{km \, s^{-1}}$ , and larger velocity gradients. However, some studies suggest that the transition between Fast and Slow events is continuous: e.g., Gaia16apd (SN 2016eay) was found to be an SLSN with LC timescale in between those of the two groups (Kangas et al. 2017).

In many cases the pre-maximum, photospheric phase spectra of Type I SLSNe can be distinguished from lower-luminosity Type Ic and BL-Ic events by a peculiar W-like absorption blend between 3900 and 4500 Å, which is identified to be due to O II (e.g., Quimby et al. 2011; Mazzali et al. 2016; Liu et al. 2017). Alternatively, this feature can be modeled using the

mixture of different ions, e.g., O III and C III (Quimby et al. 2007; Dessart 2019; Gal-Yam 2019b; Könyves-Tóth et al. 2020).

In this paper, we present ejecta mass calculations for a sample of 28 Type I SLSNe, using publicly available photometric and spectroscopic data. Our sample selection process is described in Section 3.

Recently, a similar study of SLSNe was carried out by Nicholl et al. (2015a) who inferred the ejecta mass ( $M_{\rm ej}$ ) of 24 SLSNe-I from bolometric LC modeling using the magnetar powering mechanism of the LC (Maeda et al. 2007), resulting in an average  $M_{\rm ej}$  of 10  $M_{\odot}$ , within a range of 3 and 30  $M_{\odot}$  for their sample. Yu et al. (2017) also inferred the ejecta mass of 31 SLSNe by fitting their bolometric LCs utilizing the magnetar engine model. On the other hand, from pair instability SN models (e.g., Gal-Yam 2009; Kasen et al. 2011), Lunnan et al. (2018) showed that the ejecta mass of some SLSNe may far exceed the values inferred by Nicholl et al. (2015a) from the magnetar model: for example, the initial mass of iPTF16eh was estimated to be 115  $M_{\odot}$ .

In our study the ejecta masses were inferred directly from the formulae derived by Arnett (1980) (shown in detail in Section 2), instead of full bolometric LC modeling. Our approach has the advantage of being independent of the assumed powering mechanism as long as the heating source is centrally located and the ejecta is optically thick, which are probably valid assumptions during the pre-maximum phases. Our sample of SLSNe contains 28 objects, selected by several criteria shown in Section 3.

In our calculations the photospheric velocities ( $\nu_{\rm phot}$ ) of the examined SLSNe measured before or near maximum light play a crucial role. In Section 4 we show photospheric velocity estimates for each object using a method that can provide reasonable  $\nu_{\rm phot}$  values in a computationally less expensive way than modeling all available spectra individually. We use a combination of spectrum modeling and the cross-correlation technique, similar to Liu et al. (2017) (see also, e.g., Takáts & Vinkó 2012). We also find that the W-shaped feature, typically observed in the pre-maximum spectra of SLSNe-I, is not always present, and the spectra without it seem reminiscent of SN 2015bn. We infer post-maximum photospheric velocities as well (see Section 4.5) in order to classify the studied SLSNe into the Fast or the Slow evolving SLSN-I subclasses via their velocity gradients (Inserra et al. 2018).

The ejecta mass calculations are presented in Section 5 as well as the comparison of our results with those of Nicholl et al. (2015a). We discuss our findings in Section 6, and summarize them in Section 7.

# 2. Estimating the Mass of an Optically Thick SN Ejecta

The analytical description of the light variation of SNe was first described by Arnett (1980), then extended by Arnett (1982) and Arnett & Fu (1989). This simple semi-analytical treatment has been applied for many SN subtypes including SNe II-P (Arnett & Fu 1989; Popov 1993; Nagy et al. 2014), Ia (Pinto & Eastman 2000a, 2000b), Ib/c (Valenti et al. 2008), and SLSNe (Chatzopoulos et al. 2012, 2013). Branch & Wheeler (2017) present a concise, yet in-depth summary of these analytical models (referred to as "Arnett-models" hereafter), which we follow here for our purposes.

The model assumes a homologously expanding  $(v(r) \sim r)$  ejecta having constant-density profile  $(\rho(r, t) = \rho_0 t^{-3})$ . Shortly

after explosion the ejecta is very hot, implying that radiation pressure dominates the gas pressure and the internal energy is governed by the radiation energy density ( $u \sim T^4$ ). Within this context the energy conservation law can be written as

$$\frac{du}{dt} + P\frac{dV}{dt} = \varepsilon - \frac{\partial L}{\partial m},\tag{1}$$

where  $V = 1/\rho$  is the specific volume (i.e., volume of unit mass), u is the specific internal energy,  $\varepsilon$  is the specific energy injection rate, L is the luminosity, and m is the Lagrangian mass coordinate  $(dm = 4\pi r^2 \rho dr)$ .

Another very important simplifying assumption is that the opacity of the ejecta is constant in space and also in time as long as there is no recombination. Since the density profile of the ejecta has been already set up as a constant in space, to first approximation this is a physically self-consistent assumption, if the opacity is dominated by Thomson scattering on free electrons as frequently occurs in hot SN envelopes. This assumption, however, ignores the chemical stratification within the SN ejecta which may cause significant spatial variation in the number density of free electrons even if the mass density profile is flat. See, e.g., Nagy (2018) for further details on the opacity variations in different SN types. The effect of recombination is taken into account by Arnett & Fu (1989) (see also Nagy & Vinkó 2016).

A consequence of the simplifying assumptions is that in Equation (1) the spatial and temporal parts are separable, and the solution leads to an eigenvalue problem (Arnett 1980). The temperature profile inside the ejecta has a fixed spatial profile of  $\psi(x) = \sin(\sqrt{\alpha}x)/(\sqrt{\alpha}x)$ , where  $x = r/R_{\rm SN}$  is the normalized radial coordinate and  $\alpha$  is the eigenvalue of the problem. Arnett (1980) showed that  $\alpha = \pi^2$  corresponds to the so-called "radiative zero" solution that goes to zero at the surface of the ejecta ( $\psi(1) = 0$ ). It is important to note that the Arnett-model assumes that such a temperature profile is valid as early as t = 0, which is also true for the onset of the homologous expansion. Thus, this model ignores the initial "dark phase" between the explosion and the moment of first light (e.g., Piro & Nakar 2014). This and other limitations of the Arnett-models are thoroughly discussed by Khatami & Kasen (2019).

Shortly after explosion, when the whole ejecta is hot and dense, it is optically thick, thus the photosphere is located near the outer boundary (denoted as  $R_{\rm SN}$  above). Photons that are generated inside the ejecta, regardless of the physical nature of the powering mechanism, must diffuse out to the photosphere in order to escape. Following Arnett (1980), the timescale of the photon diffusion can be expressed as

$$t_{\rm d} = \frac{3R_{\rm SN}^2 \rho \kappa}{\alpha c},\tag{2}$$

where  $\alpha = \pi^2$  is the eigenvalue of the radiative zero solution. In the diffusion approximation the luminosity inside the ejecta is

$$L(r) = -4\pi r^2 \frac{\lambda c}{3} \frac{du}{dr} = -4\pi r^2 \frac{c}{3\kappa\rho} \frac{du}{dr},\tag{3}$$

where  $\lambda = (\kappa \ \rho)^{-1}$  is the photon mean free path. Equation (3) is similar to the expression for radiative energy transport within stellar interiors.

The other characteristic timescale of the problem is the expansion timescale (also called as "hydrodynamic timescale")

which is simply

$$t_h = \frac{R_{\rm SN}}{v_{\rm SN}},\tag{4}$$

where  $v_{\rm SN}$  is the expansion velocity at  $R_{\rm SN}$ . Since real SN ejecta have no constant-density profiles,  $v_{\rm SN}$  cannot be related unambiguously to measured SN velocities. Therefore, it is often referred to as the "scaling velocity" that characterizes only the approximate analytic solution.

Since  $R_{\rm SN} \sim t$  while  $\rho \sim t^{-3}$ ,  $t_d \sim t^{-1}$  is decreasing in time while  $t_h \sim t$  is increasing. At the start of the expansion  $t_d \gg t_h$ , thus later there is a moment when  $t_d$  and  $t_h$  become equal. At this moment the diffusing photons have the same effective speed as the expanding ejecta, thus the thermalized photons from the instantaneous energy input (the heating source) are no longer trapped inside the ejecta. In other words, the escaping luminosity is equal to the instantaneous energy input, which occurs when the luminosity reaches its maximum,  $L_{\rm max}$  ("Arnett's rule"; see also Khatami & Kasen 2019). If  $t_{\rm max}$  is the moment of maximum light in the observer's frame, and  $t_0$  denotes the moment of explosion (actually the moment of the start of homologous expansion, see above), then the rise time to maximum light in the SN rest frame is

$$t_{\text{rise}} = \frac{t_{\text{max}} - t_0}{1 + z},$$
 (5)

where *z* is the redshift of the SN.

It must be emphasized that "Arnett's rule," in its original form introduced above specifies only the moment of maximum light with respect to the start of the expansion, irrespective of the actual powering mechanism inside the SN ejecta. It is a consequence that it also allows the determination of the actual value of  $L_{\text{max}}$  once the powering mechanism is known. This works, for example, in the case of SNe Ia, where the heating is thought to be entirely due to the decay of radioactive <sup>56</sup>Ni, and enables the derivation of the initial amount of <sup>56</sup>Ni that is needed to power the observed LC. This is, however, not the case for SLSNe, where the powering mechanism is still debated and does not seem to be due to Ni-decay (e.g., Chatzopoulos et al. 2013). Thus, in this paper we do not make any assumption on the powering mechanism of SLSNe, and use "Arnett's rule" only to estimate the physical conditions in the ejecta around maximum light.

Close to  $t_{\text{max}}$ , when  $t_d \approx t_h$ , the optical depth of the whole constant-density ejecta can be written as (Branch & Wheeler 2017)

$$\tau = \kappa \rho R_{\rm SN} = \frac{\pi^2 c}{3\nu_{\rm SN}} \approx \frac{3c}{\nu_{\rm SN}}.$$
 (6)

Because  $c \gg v_{\rm SN}, \ \tau \gg 1$ , i.e., at  $t \sim t_{\rm max}$  most of the ejecta is still optically thick, as expected. As a consequence, the photosphere, where the ejecta becomes transparent, must be located close to  $R_{\rm SN}$ , i.e.,  $R_{\rm phot} \approx R_{\rm SN}$ .

Equation (6) allows the possibility of estimating the ejecta mass, in particular the mass of the optically thick part inside the photosphere (e.g., Könyves-Tóth et al. 2020). Due to the constant-density profile,  $\rho = 3M_{\rm ej}(4\pi)^{-1}R_{\rm phot}^{-3}$ . Inserting this into Equation (6) we have

$$M_{\rm ej} = 4\pi \frac{c}{\kappa} v_{\rm ph} t_{\rm rise}^2, \tag{7}$$

where we used the photospheric velocity at maximum light,  $v_{\rm ph}$ , to approximate the scaling velocity,  $v_{\rm SN}$ , of the optically thick ejecta, and  $R_{\rm ph} = v_{\rm ph}t_{\rm rise}$  in the SN rest frame.

Equation (7) is very similar to the original expression introduced by Arnett (1980), which gives the total ejecta mass from the "mean light-curve timescale"  $t_m = \sqrt{2t_h t_d}$  in the following form:

$$M_{\rm ej} = \frac{\beta c}{2\kappa} v_{\rm SN} t_m^2, \tag{8}$$

where  $\beta \approx 13.8$  is an integration constant, slightly depending on the ejecta density profile. Even though  $t_m$  cannot be measured directly, its value is similar to the rise time of the LC, thus Equations (7) and (8) provide approximately the same ejecta mass for a given SN, with the systematic difference of a constant multiplier: the quotient of the two formulae is

$$4\pi \cdot \frac{2}{\beta} = 1.82. \tag{9}$$

In the rest of this paper we apply Equations (7) and (8) to observational data of SLSNe-I to derive constraints for their ejecta mass. Again, we note that these estimates do not make any assumption on the physics of the powering mechanism (magnetar, radioactivity, etc.) as long as the heating source is centrally located, thus the thermalized photons must diffuse through the whole ejecta.

# 3. Sample Selection

We constructed a sample of SLSNe from the events listed in the Open Supernova Catalog (OSC)<sup>4</sup> (Guillochon et al. 2017) before 2020, which has at least 10 epochs of observed photometric data. From the identified 98 objects, 18 were immediately excluded from the sample owing to being Type II SLSNe. As the main goal of this study is to determine the ejecta masses of Type I SLSNe using Equations (7) and (8), spectra taken before or shortly after the moment of the maximum light are crucial to identify the typical SLSN-I features and estimate the value of the photospheric velocity  $(v_{phot})$ . Without knowing v<sub>phot</sub> at maximum, the ejecta mass calculations based on the formulae presented in Section 2 would not lead to reasonable results. Out of the pre-selected 80 SLSNe-I, 39 did not pass the criterion of possessing pre-maximum spectra. From the remaining 41 objects, 13 additional SLSNe-I had to be removed from the sample for several reasons listed in the Appendix. All SLSNe excluded from our analysis are collected in Table A1 in the Appendix, for completeness.

Table 1 contains the basic observational data of our final sample (28 SLSNe) obtained from the OSC. The moment of explosion ( $t_0$ ) was estimated by fitting an LC model via the Modular Open Source Fitter for Transients code (Nicholl et al. 2017c) to the LCs as provided by the OSC.

Before the analysis, all downloaded spectra were normalized to the flux at 6000 Å, and corrected for redshift and Milky Way extinction.

# 4. Photospheric Velocity Measurement

In this section, we describe a method for estimating the photospheric velocity of SLSNe-I in our sample. The  $v_{\text{phot}}$ 

https://spe.space

**Table 1**Basic Data of the Studied SLSNe

SLSN	t <sub>0</sub> MJD	t <sub>max</sub> MJD	M <sub>max</sub> (mag)	R.A.	Decl.	z	E(B-V) (mag)	References
SN2005ap	53415	53440	18.16	13:01:14.8	+27:43:31.4	0.2832	0.0072	1, 2, 3, 4, 5
SN2006oz	54033	54068	19.80	22:08:53.6	+00:53:50.4	0.3760	0.0403	2, 5, 6, 7, 8
SN2010gx	55246	55277	17.62	11:25:46.7	-08:49:41.4	0.2299	0.0333	1, 2, 9, 10, 11, 12
SN2010kd	55499	55552	16.16	12:08:01.1	+49:13:31.1	0.1010	0.0197	1, 2, 10, 13
SN2011kg	55907	55938	18.39	01:39:45.5	+29:55:27.0	0.1924	0.0371	2, 9, 10, 11, 14, 15, 16
SN2015bn	57000	57101	15.69	11:33:41.6	+00:43:32.2	0.1136	0.0221	2, 17, 18
SN2016ard	57424	57454	18.39	14:10:44.6	-10:09:35.4	0.2025	0.0433	2, 19, 20
SN2016eay	57509	57530	15.20	12:02:51.7	+44:15:27.4	0.1013	0.0132	2, 21, 22
SN2016els	57578	57605	18.31	20:30:13.9	-10:57:01.8	0.2170	0.0467	2, 10, 23
SN2017faf	57908	57941	16.78	17:34:40.0	+26:18:22.0	0.0290	0.0482	2, 24, 25
SN2018bsz	58197	58275	13.99	16:09:39.1	-32:03:45.7	0.02667	0.2071	2, 26, 27, 28
SN2018ibb	58336	58466	17.66	04:38:57.0	-20:39:44.0	0.1600	0.0284	2, 29
SN2018hti	58383	58486	16.46	03:40:53.8	+11:46:37.3	0.0630	0.4129	2, 30, 31
SN2019neq	58700	58731	17.79	17:54:26.7	+47:15:40.6	0.1075	0.0285	32, 33, 34
DES14X3taz	57021	57093	20.54	02:28:04.5	-04:05:12.7	0.6080	0.0220	2, 35, 36
iPTF13ajg	56348	56430	19.26	16:39:04.0	+37:01:38.4	0.7400	0.0121	2, 11, 37
iPTF13ehe	56565	56676	19.6	06:53:21.5	+67:07:56.0	0.3434	0.0434	2, 11, 38
LSQ12dlf	56098	56150	18.46	01:50:29.8	-21:48:45.4	0.2550	0.0110	2, 39, 40, 41, 42
LSQ14an	56639	56660	18.60	12:53:47.8	-29:31:27.2	0.1630	0.0711	2, 43, 44, 45
LSQ14mo	56659	56693	18.42	10:22:41.5	-16:55:14.4	0.2530	0.0646	2, 10, 46, 47
LSQ14bdq	56735	56798	19.16	10:01:41.6	-12:22:13.4	0.3450	0.0559	2, 48, 49
PS1-14bj	56597	56808	21.19	10:02:08.4	+03:39:19.0	0.5215	0.0205	2, 50, 51, 52
PTF09atu	54999	55062	19.91	16:30:24.6	+23:38:25.0	0.5015	0.0409	2, 9, 11, 16, 53, 54, 55
PTF09cnd	55017	55085	17.08	16:12:08.9	+51:29:16.1	0.2584	0.0207	9, 10, 11, 16, 39, 55
PTF10nmn	55267	55385	18.52	15:50:02.8	-07:24:42.5	0.1237	0.1337	2, 9, 11, 16, 53
PTF12dam	56021	56091	15.66	14:24:46.2	+46:13:48.3	0.1074	0.0107	2, 9, 10, 11, 16, 56, 57
PTF12gty	56082	56139	19.45	16:01:15.2	+21:23:17.4	0.1768	0.0600	2, 11, 16, 53
SSS120810	56122	56159	17.38	23:18:01.8	-56:09:25.6	0.1560	0.0158	2, 40, 41, 58, 59

References. (1) Lennarz et al. (2012); (2) Schlafly & Finkbeiner (2011); (3) Puckett et al. (2005); (4) Modjaz et al. (2005); (5) Quimby et al. (2007); (6) Leloudas et al. (2012); (7) Bassett et al. (2006); (8) Green (2006); (9) Perley et al. (2016); (10) Brown et al. (2014); (11) Yaron & Gal-Yam (2012); (12) Pastorello et al. (2010a); (13) Kumar et al. (2020); (14) Ofek et al. (2013); (15) Quimby et al. (2013); (16) Quimby et al. (2018); (17) Nicholl et al. (2016b); (18) Le Guillou et al. (2015); (19) Chornock et al. (2016); (20) Blanchard et al. (2018b); (21) Nicholl et al. (2017a); (22) Kangas et al. (2016); (23) Fraser et al. (2016); (24) Pastorello et al. (2017); (25) Kilpatrick (2017); (26) Blanchard et al. (2018a); (27) Anderson et al. (2018); (28) Hiramatsu et al. (2018); (29) Pursiainen et al. (2018); (30) Burke et al. (2018); (31) Tonry et al. (2018); (32) Nordin et al. (2019); (33) Perley (2019); (34) Könyves-Tóth et al. (2020); (35) Smith et al. (2016); (36) Castander et al. (2015); (37) Vreeswijk et al. (2014); (38) Yan et al. (2015); (39) Shivvers et al. (2019); (40) Smartt et al. (2015); (41) Nicholl et al. (2014); (42) Smartt et al. (2012); (43) Inserra et al. (2017); (44) Leget et al. (2014); (45) Smartt et al. (2015); (46) Leloudas et al. (2014a); (47) Chen et al. (2017a); (48) Nicholl et al. (2015b); (49) Benitez et al. (2014); (50) Lunnan et al. (2016); (51) Lunnan et al. (2018); (52) Nicholl et al. (2016a); (53) Neill et al. (2011); (54) De Cia et al. (2018); (55) Chandra et al. (2009); (56) Levan et al. (2013); (57) Quimby et al. (2012); (58) Wright et al. (2012); (59) Drake et al. (2009).

value before or near the moment of maximum light plays a major role in the ejecta mass calculations (see Section 2). Post-maximum photospheric velocities are needed also in order to infer velocity gradients, and classify these events into the Fast or the Slow evolving SLSN-I subgroups.

However, getting realistic  $v_{\rm phot}$  estimates is not a trivial problem, as a typical SLSN spectrum contains broad and heavily blended features instead of isolated and easily identifiable P Cygni profiles. In this case a spectrum synthesis code is required to reliably identify the spectroscopic features and the ejecta composition, but even this method suffers from ambiguity: occasionally, the absorption blends can be fitted equally well with features of different ions (see, e.g., Könyves-Tóth et al. 2020). Furthermore, modeling each available spectrum in our sample would be very time consuming. Thus, in Section 4.1 we present a faster and reasonably accurate method by combining spectrum synthesis and cross-correlation (see also, e.g., Takáts & Vinkó 2012; Liu et al. 2017) to estimate the  $v_{\rm phot}$  of the 28 SLSNe we studied.

#### 4.1. Methodology

According to, e.g., Quimby et al. (2018), and Perley et al. (2019), a W-shaped absorption feature appearing between ~3900 and ~4500 Å is typically present in the pre-maximum spectra of Type I SLSNe. It is usually modeled as a blend of O II lines, and assumed to appear in all spectra of Type I SLSNe. Liu et al. (2017) examined a large set of normal and SLSNe, and noticed that this W-shaped O II feature can be found in all Type I SLSNe, but is missing from the spectrum of normal Type Ic or broad-lined Ic SNe. They proposed the presence/absence of the W-feature as a tool for distinguishing between SLSNe and normal Ic SN events using only premaximum spectra.

Motivated by these previous findings, we assumed that the W-shaped feature plays a significant role in the spectrum formation of all SLSNe in our sample. We built a series of SYN ++ models (Thomas et al. 2011) containing only O II features (see Figure 1). These models share the same local parameters, e.g., the photospheric temperature ( $T_{\rm phot}$ ) of 17,000 K, but have

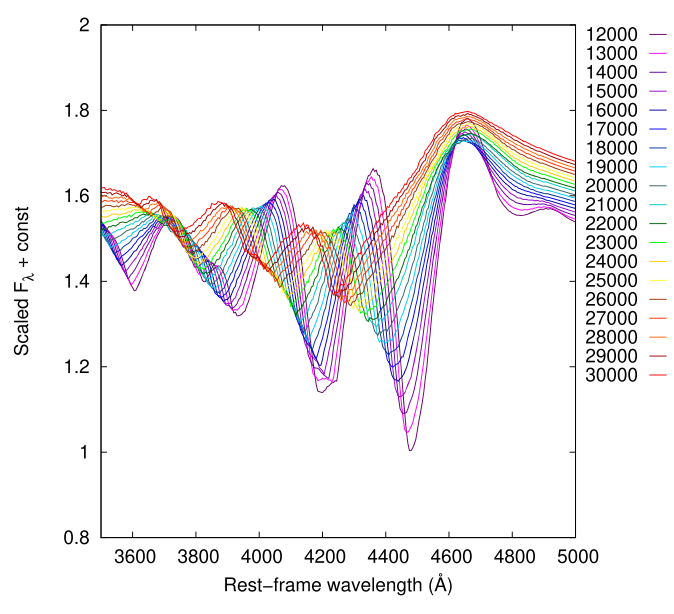


**Figure 1.** SYN++ models built with  $T_{\rm phot} = 17,000~{\rm K}$  for the W-shaped O II blend appearing typically between 3900 and 4500 Å in the pre-maximum spectra Type I SLSNe. Different colors code the models having different  $v_{\rm phot}$  values ranging from 10,000 to 30,000 km s<sup>-1</sup>.

different  $v_{\rm phot}$  values ranging from 10,000 to 30,000 km s<sup>-1</sup>, as shown in Figure 1 with different colors. The fixed value of all global ( $a_0$ ,  $v_{\rm phot}$ ,  $T_{\rm phot}$ ) and local (log  $\tau$ ,  $v_{\rm min}$ ,  $v_{\rm max}$ , aux,  $T_{\rm exc}$ ) SYN++ model parameters can be found in Table A2 in the Appendix. Here, we utilize the name *global* to the parameters referring to the whole model spectrum, and *local* to those fitting the lines of individual elements in the spectrum.

Next, we cross-correlated the O II models with each other using the fxcor task in the onedspec.rv package of IRAF<sup>5</sup> (Image Reduction and Analysis Facility). We chose the model corresponding to  $v_{\text{phot}} = 10,000 \,\text{km s}^{-1}$  as the template spectrum, and computed the cross-correlation velocity differences  $(\Delta v_{\rm X})$  between the template and all other model spectra. Then, by comparing  $\Delta v_{\rm X}$  with the real velocity differences between the models ( $\Delta v_{\text{phot}}$ ), we obtained a formula to convert the velocity differences inferred by fxcor to real, physical velocity differences between the SYN++ models. Having this correction formula we are able to use the cross-correlation method to determine reliable velocities for the observed spectra, despite the well-known issues with applying crosscorrelation to spectra with P Cygni features (e.g., Takáts & Vinkó 2012). Our method is similar to that developed by Liu et al. (2017), but we focused on the more pronounced premaximum O II features in the model instead of the Fe II  $\lambda 5169$ feature in post-maximum spectra.

Afterwards, we cross-correlated the 28 observed spectra in the sample with the template O II model spectrum (i.e., the one having  $v_{\rm phot}=10,\!000\,{\rm km\,s}^{-1}$ ). We derived  $v_{\rm phot}$  for the observed spectra by getting  $\Delta v_{\rm X}$  from fxcor, then applying the correction formula between  $\Delta v_{\rm phot}$  and  $\Delta v_{\rm X}$  (see above). As a cross-check, we also plotted together the observed spectra with the SYN++ model having the nearest  $v_{\rm phot}$  to the corrected velocity from fxcor (see Sections 4.3 and 4.4).

## 4.2. New Subtypes of SLSNe-I

Applying the method described above, we found that it did not work for about one-third of the sample, i.e., their derived photospheric velocities turned out to be physically impossible. Closer inspection of those spectra revealed the cause of this inconsistency: the W-shaped O II feature was not present in their spectra at all, therefore the cross-correlation process did not work properly.

After collecting the spectra without the W-shaped absorption feature, we found that they were similar to each other. The best-observed prototype of these SLSNe is SN 2015bn.

Thus, we define two distinct groups of Type I SLSNe in our sample, characterized by the presence/absence of the W-shaped O II feature between 3900 and 4500 Å. Hereafter we refer to them as "Type W" and "Type 15bn" SLSNe (see Table 3).

Note that the presence of these subgroups is not validated by a quantitative statistical procedure, either a classical clustering method or machine-learning algorithm, because there are too few SLSNe in our sample to analyze them statistically. However, it is seen that the Type 15bn sample contains objects having mostly pre-maximum spectra, ranging from -42 to -1 days in rest-frame. None of them show the W-like feature, unlike the objects in the Type W subgroup. The W-like feature usually appears in the pre-maximum spectra in the latter sample. Although the Type 15bn sample is still poor, there seems to be a strong indication that these SLSNe (at least the observed ones) do not contain the W-like absorption blend.

The observed spectra taken before maximum of all "Type W" SLSNe can be seen in Figure 2, while the same for "Type 15bn" events are shown in Figure 3 with different colors representing each object in the given subclass.

For the latter subclass, we estimated their correct  $v_{\rm phot}$  values by applying a different SYN++ model template in the cross-correlation process. The formula for correcting their  $\Delta v_{\rm X}$  to  $\Delta v_{\rm phot}$  was also re-calculated accordingly.

Further details on the cross-correlation analysis of Type W and Type 15bn SLSNe are given in Sections 4.3 and 4.4, respectively.

In Section 4.5, we present the  $v_{\rm phot}$  estimates after the maximum for nine objects in our sample, which had observational data between +25 and +35 rest-frame days after maximum besides the pre-maximum data. Although e.g., Gal-Yam (2012) and Inserra et al. (2018) defined the Fast and the Slow evolving subgroup of Type I SLSNe by their LC evolution timescales, the date of explosion is weakly defined in several cases, thus the rise time of these SLSNe remains uncertain. Therefore we utilized the photospheric velocity evolution by ~30 days after the maximum for classification (see the details in Section 4.6).

## 4.3. Type W SLSNe

The real, physical velocity differences ( $\Delta v_{\rm phot}$ ) between the models having  $v_{\rm phot}$  ranging from 10,000 to 30,000 km s<sup>-1</sup> and the template model spectrum of 10,000 km s<sup>-1</sup> can be seen in Figure 4 as a function of the velocity difference calculated by the fxcor task in IRAF ( $\delta v_{\rm X}$ ). The data for the "Type W" subclass (red circles) were fitted by a second-order polynomial as

$$\Delta v_{\text{phot}} = a_0 + a_1 \cdot \Delta v_X + a_2 \cdot \Delta v_X^2, \tag{10}$$

<sup>&</sup>lt;sup>5</sup> IRAF is distributed by the National Optical Astronomy Observatories, which are operated by the Association of Universities for Research in Astronomy, Inc., under cooperative agreement with the National Science Foundation. http://iraf.noao.edu.

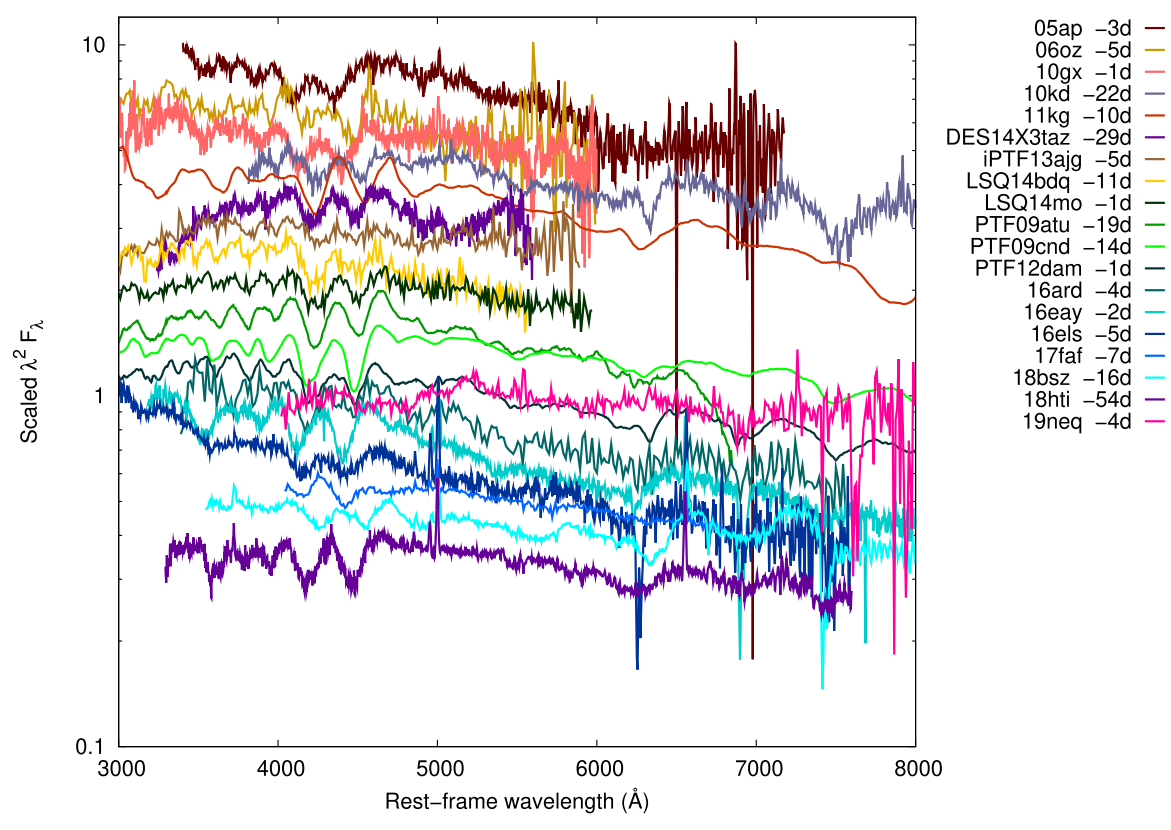


Figure 2. Observed pre-maximum spectra of Type W SLSNe. The colors code the individual objects, and the spectra are shifted vertically for clarity.

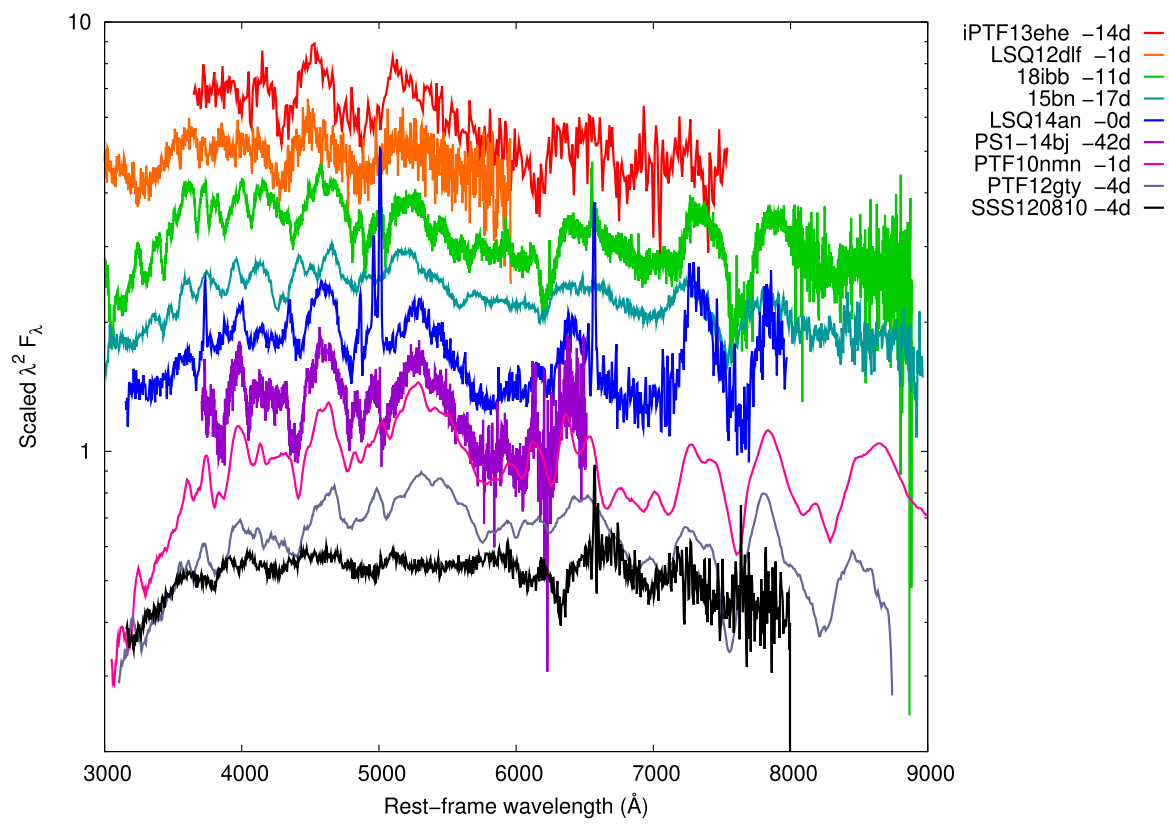
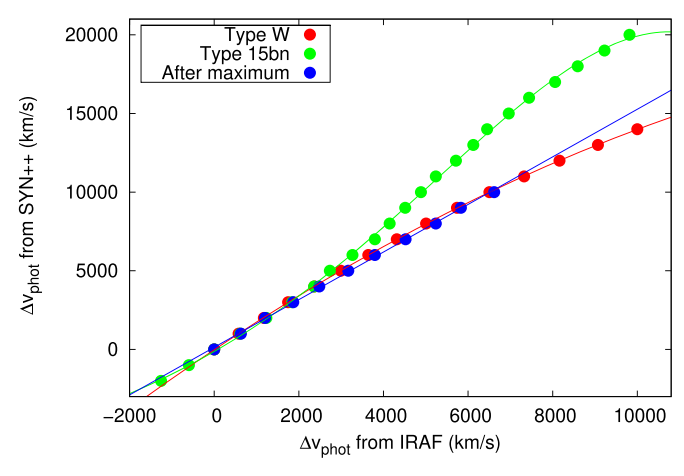


Figure 3. Observed pre-maximum spectra of Type 15bn SLSNe. The colors code the individual objects, and the spectra are shifted vertically for clarity.



**Figure 4.** Comparison of the relative velocities between the SYN++ models and the template model given by fxcor ( $\Delta \nu_X$ , horizontal axis) and the real velocity differences between the model  $\nu_{phot}$  values ( $\Delta \nu_{phot}$ , vertical axis). Red and green colors represent the models for the Type W and Type 15bn subclasses, respectively, while the blue symbols correspond to the post-maximum spectra. The best-fit polynomials are also shown (see the text).

and obtained  $a_0 = 155.01 \ (\pm 82.64)$ ,  $a_1 = 1.68 \ (\pm 0.03)$ , and  $a_2 = -2.78 \times 10^{-5} \ (\pm 1.63 \times 10^{-6})$ .

Finally, after cross-correlating the observed spectra with the model template, we applied Equation (10) to infer the final  $v_{\rm phot}$  values, which are shown in Table 3, together with epochs of the observations and their rest-frame phases.

In Figure 5, the observed pre-maximum spectra of the Type W sample are plotted with black lines, together with the best-fit SYN++ model spectrum (green line) that has the most similar photospheric velocity to the inferred  $v_{\rm phot}$ . Note that since this analysis aims at measuring only the expansion velocity, the spectra appearing in Figure 5 are flattened, and neither the continuum nor the feature depths are fitted. Thus, only the wavelength positions of the features are expected to match.

# 4.4. Type 15bn SLSNe

For each object belonging to the Type 15bn subclass, the photospheric velocity was determined using the same method as discussed in Section 4.3. However, in this case the modeling of the the whole optical spectrum was necessary to get reliable estimates for  $v_{\rm phot}$ , since no typical and easily identifiable feature can be found in those spectra in contrast with the Type W SLSNe.

Therefore, we built a SYN++ model to describe the spectrum of a well-observed representative of the Type 15bn group, which was selected to be SN 2018ibb. The observed spectrum of SN 2018ibb taken at -11 rest-frame days relative to maximum light can be seen in the left panel of Figure A1 in the Appendix (black line), together with its best-fit SYN++ model (red line). The single-ion contributions to the overall model spectrum are also presented as orange curves, shifted vertically for better visibility. The photospheric temperature and velocity of the best-fit model are  $T_{\rm phot} = 11,000$  K and  $v_{\rm phot} = 8000$  km s<sup>-1</sup>, respectively. The spectrum contains C II, O I, Mg II, Si II, Ca II, Fe II, and Fe III ions. The full set of the global and local parameter values for the SN 2018ibb model can be found in Table A2 in the Appendix.

Thereafter, we synthesized model spectra with the same local and global parameters as the best-fit SYN++ model of the premaximum spectrum of SN 2018ibb, but having different  $v_{\rm phot}$  in between 8000 and 30,000 km s<sup>-1</sup> (see Figure 6). These models were cross-correlated with that having  $v_{\rm phot} = 10,000 \, {\rm km \, s^{-1}}$ . Then, a similar correction formula between the velocity differences was computed as previously, resulting in

$$\Delta v_{\text{phot}} = a_0 + \sum_{n=1}^4 a_n \cdot \Delta v_X^n, \tag{11}$$

with  $a_0 = -128.61 (\pm 79.92)$ ,  $a_1 = 1.53 (0.06)$ ,  $a_2 = 1.09 \times 10^{-4} (3.88 \times 10^{-5})$ ,  $a_3 = 5.45 \times 10^{-9} (7.44 \times 10^{-9})$ , and  $a_4 = -1.16 \times 10^{-12} (4.27 \times 10^{-13})$ .

The resulting  $\Delta v_{\text{phot}}$  values are plotted with green dots in Figure 4, and the best-fit polynomial (Equation (11)) is shown also with a green line.

Finally, after applying Equation (11) to the observed premaximum spectra in the Type 15bn subclass, the  $v_{\rm phot}$ velocities are collected in Table 3.

The observed pre-maximum spectra of Type 15bn SLSNe are shown in Figure 7 with black lines, together with the best-fit SYN++ model for SN 2018ibb (green) Doppler-shifted to the inferred  $v_{\rm phot}$  for each object.

It is seen in Table 3 that SLSNe in the Type 15bn group have lower photospheric velocities compared to the Type W SLSNe in general. This suggests that Type 15bn SLSNe are similar to each other, not only in the appearance of their spectra, but also in their  $T_{\rm phot}$  and  $v_{\rm phot}$  parameters. It is suspected that they are forming a subgroup of SLSNe-I that is different from the Type W subclass, because the latter have faster ejecta expansion velocities and hotter photospheres during the pre- and near-maximum phases. In Sections 5 and 6, we discuss additional differences between these two subclasses in detail.

#### 4.5. Post-maximum Spectra

In order to classify the events in our sample into the Fast or the Slow evolving subgroup of Type I SLSNe, photospheric velocities determined from the spectra taken at  $\sim+30$  rest-frame days after maximum are required (Inserra et al. 2018). By comparing the post-maximum velocities to the  $v_{\rm phot}$  estimated near the moment of maximum light, it can be decided unambiguously if an SLSN belongs to the Fast or the Slow SLSNe-I.

From the 28 SLSNe in our sample, nine possessed post-maximum spectra between the +25 and +35 day phases, and both Type W and Type 15bn objects were represented among them,. These spectra are collected and shown in Figure 8.

From the available post-maximum spectra, the one taken at the +30 rest-frame day phase of SN 2015bn was chosen for modeling. It can be seen together with its best-fit SYN++ model in the right panel of Figure A1 in the Appendix, with the same color coding as the model of SN 2018ibb. The best-fit model was found to have  $T_{\rm phot} = 9000$  K and  $v_{\rm phot} = 8000$  km s<sup>-1</sup>, and it contains O I, Na I, Mg II, Si II, Si II v, Ca II, and Fe II ions. The "v" next to Si II refers to the high velocity of this feature. It has higher velocity than  $v_{\rm phot}$ , as it is formed above the photosphere in the outer regions of the SN ejecta. The parameters of the best-fit SYN++ model can be found in Table A2 in the Appendix.

Since the  $v_{\text{phot}}$  of an expanding SN atmosphere decreases with time as the ejecta becomes more and more transparent, in

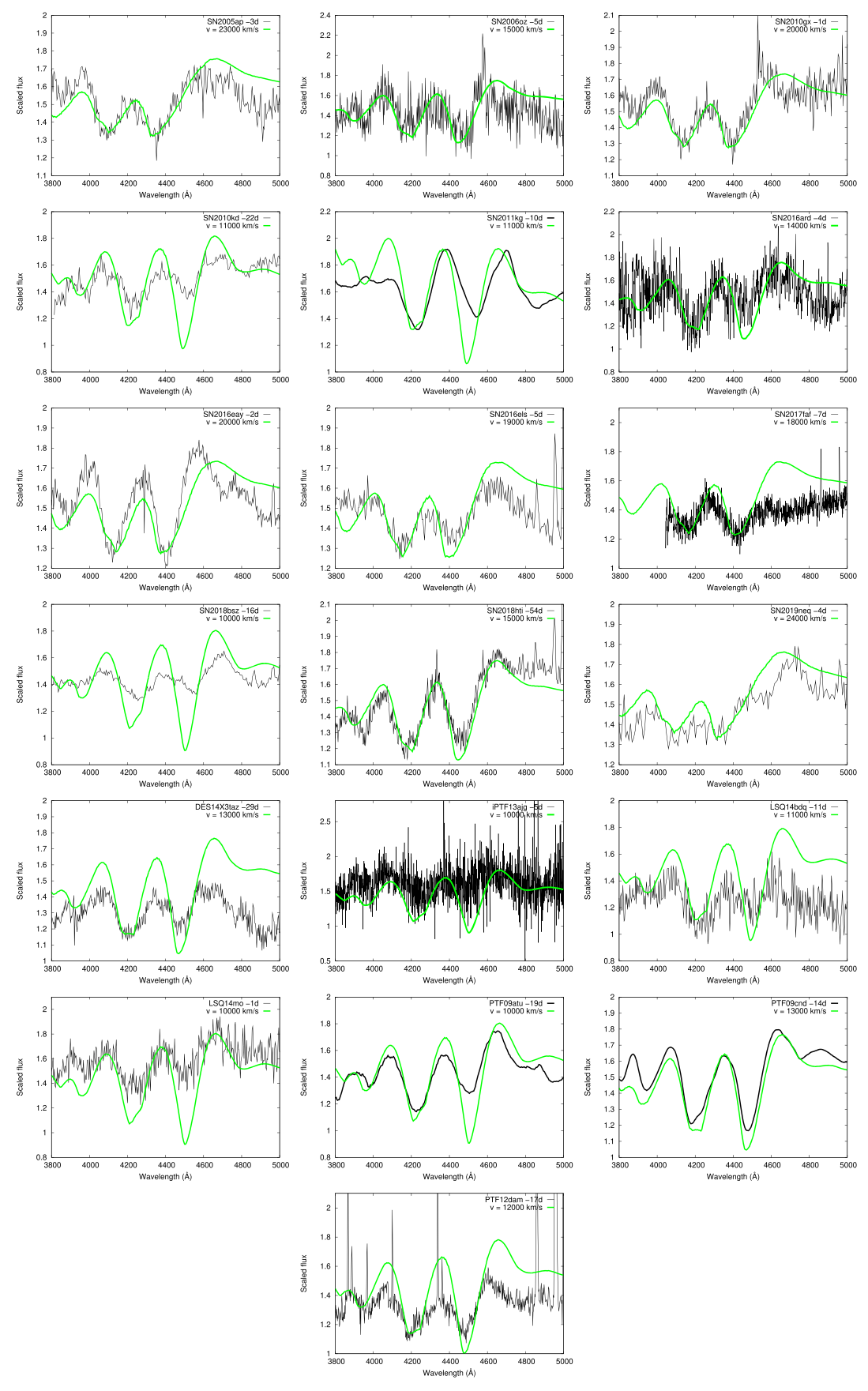


Figure 5. Observed pre-maximum spectra of Type W SLSNe (black), together with their best-fit O II model spectra obtained in SYN++ (green).

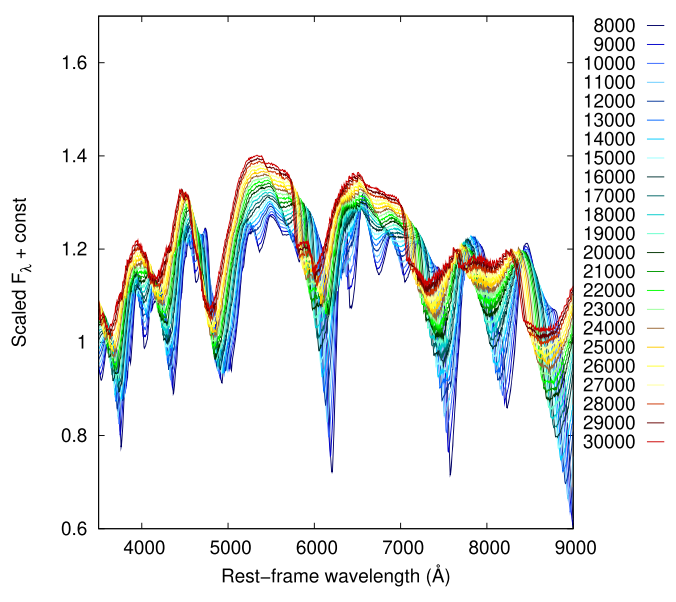


Figure 6. SYN++ models of Type 15bn SNe having  $T_{\text{phot}} = 11,000 \text{ K}$  and  $v_{\text{phot}}$  ranging between 8000 and 30,000 km s<sup>-1</sup>.

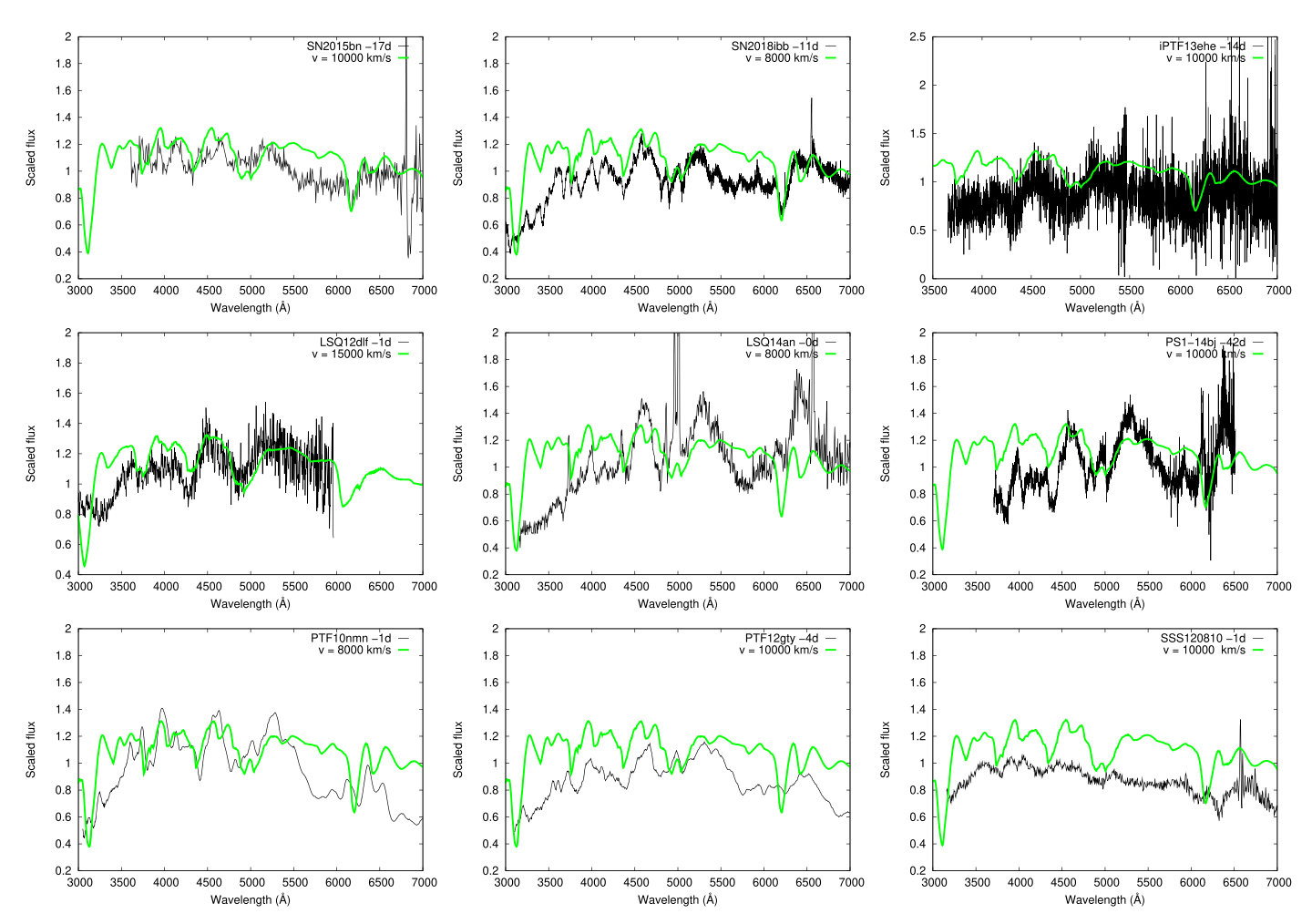


Figure 7. Observed pre-maximum spectra of Type 15bn SLSNe (black), together with the Doppler-shifted best-fit model built for SN 2018ibb (green) in accordance with the inferred  $\nu_{phot}$  for each object.

the case of the post-maximum spectra we utilized and crosscorrelated models having lower velocities compared to those built for the pre-maximum phases. We created 11 variants of the best-fit model of the +30 day phase spectrum of SN 2015bn, with  $v_{\rm phot}$  between 5000 and 15,000 km s<sup>-1</sup> (see Figure 9). After cross-correlating them, we

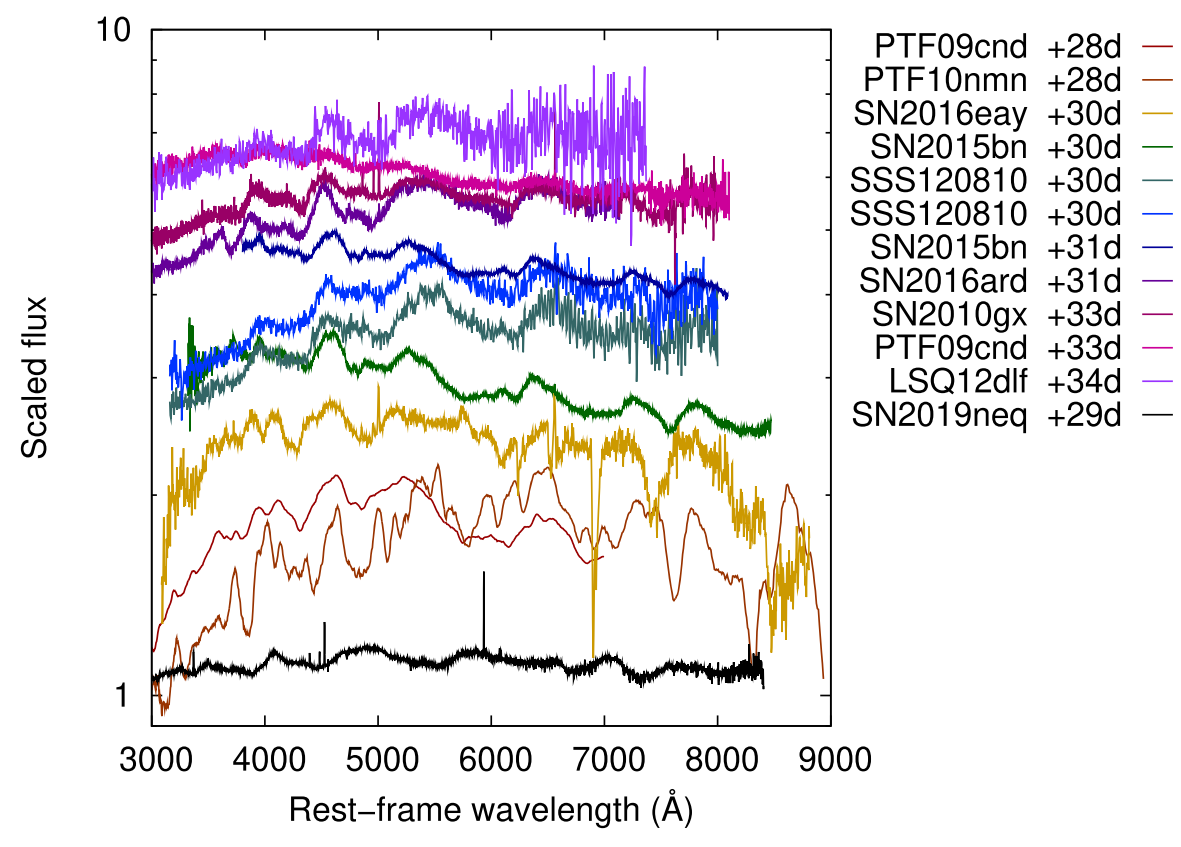
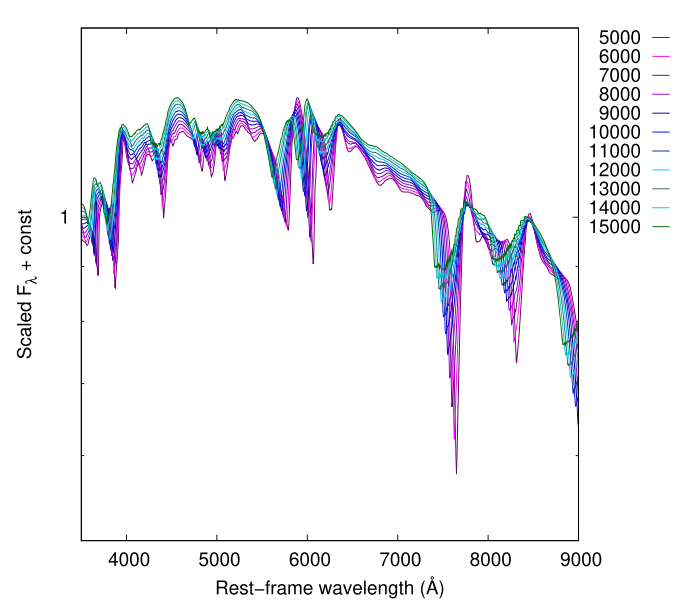


Figure 8. Spectra taken between the +25 and +35 day rest-frame phases after maximum light for nine SLSNe in our sample.



**Figure 9.** SYN++ models having  $T_{\rm phot} = 11,000 \, \rm K$  and  $\nu_{\rm phot}$  between 5000 and 15,000 km s<sup>-1</sup> for the spectra taken around  $\sim$ 30 days after maximum.

reached a similar velocity correction formula, as discussed in Sections 4.3 and 4.4, namely

$$\Delta v_{\text{phot}} = a_0 + a_1 \Delta v_{\text{X}} \tag{12}$$

with  $a_0 = 135.62 \pm 54.81$ ) and  $a_1 = 1.51 \pm 0.01$ ). The data as well as the best-fit straight line are shown in Figure 4 in blue. Afterwards, we cross-correlated the observed post-maximum spectra with the +30 day phase spectrum of SN 2015bn,

instead of a SYN++ model, and then Doppler-shifted them with the  $\Delta \nu_{phot}$  differences from SN 2015bn calculated via fxcor and Equation (12). Figure 10 displays the available post-maximum spectra of the nine SLSNe in our sample (black), together with the +30 day phase spectrum of SN 2015bn Doppler-shifted with the velocity difference obtained with IRAF for each object (green). The best-fit SYN++ model for SN 2015bn having  $\nu_{phot} = 8000 \, \mathrm{km \, s^{-1}}$ , and the best-fit model referring to the particular SLSN, are also plotted with purple and magenta curves, respectively.

The photospheric velocity estimates for the post-maximum phase spectra of the nine available objects can be found in Table 2.

# 4.6. Fast/Slow Classification

In the case of the nine events for which both pre- and post-maximum spectra were available, the classification into the Fast or Slow category was unambiguous. The estimated  $v_{\rm phot}$  values before and after maximum can be found in Table 2.

Figure 11 displays the photospheric velocity evolution of the nine SLSNe as a function of rest-frame phase relative to the moment of the maximum light. It is seen that SN 2010gx, SN 2016eay, and SN 2019neq show a factor of 2 higher  $\nu_{\rm phot}$  near maximum than the rest of the sample, which decreases swiftly in the post-maximum phases. By  $\sim\!30$  days after maximum their velocities become similar to those of the other six SLSNe. These rapidly evolving objects are plotted with different tones of red in Figure 11, and they will be referred to as Fast (F) SLSNe-I from now. The fast evolution of these objects is consistent with previous studies (e.g., Pastorello et al. 2010b; Inserra et al. 2018; Könyves-Tóth et al. 2020).

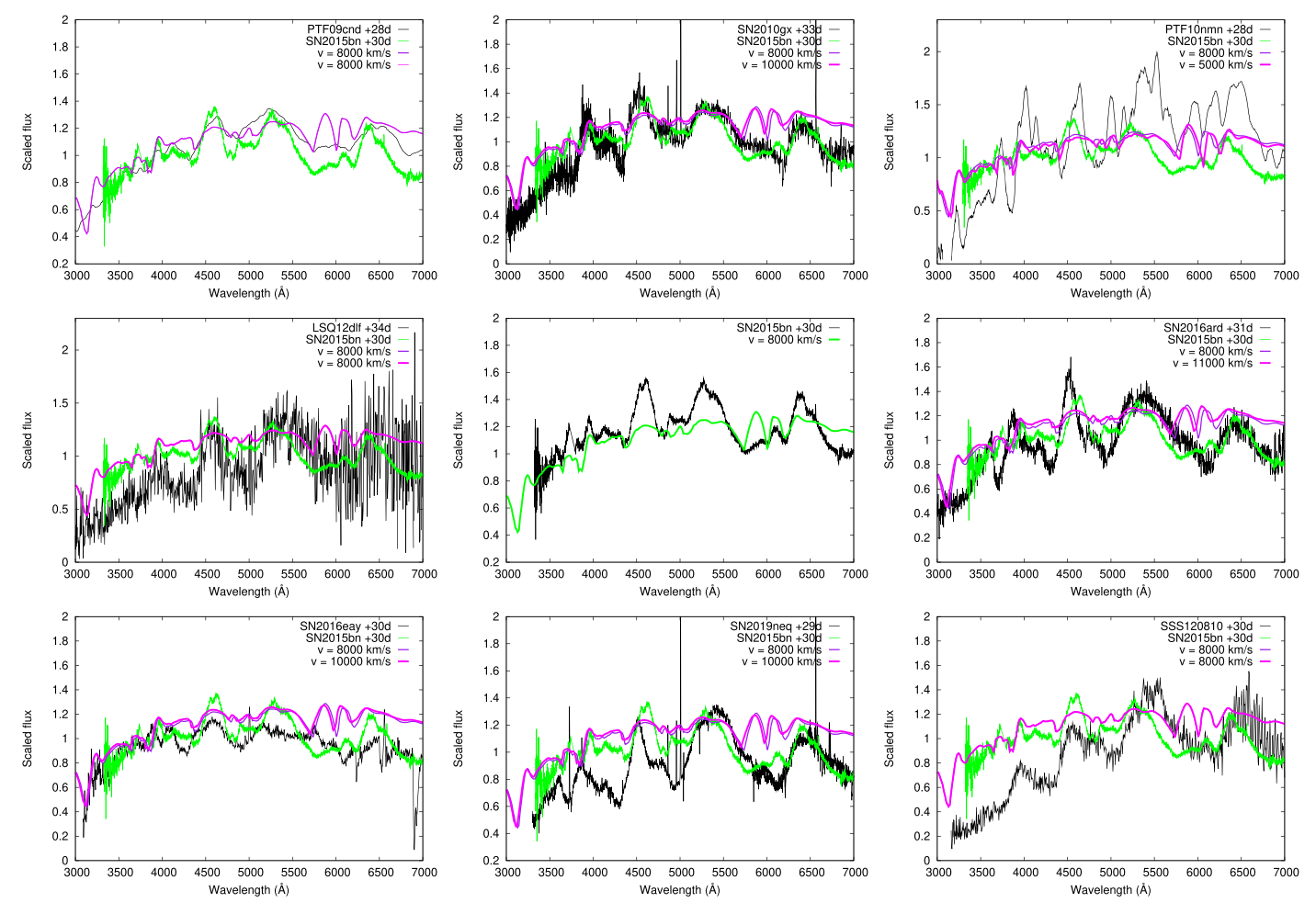


**Figure 10.** Available post-maximum spectra of nine SLSNe in our sample (black), with the +30 day phase spectrum of SN 2015bn Doppler-shifted with the velocity difference obtained with IRAF (green). The purple curves refer to the best-fit SYN++ model for SN 2015bn, but Doppler-shifted to  $v_{phot} = 8000 \text{ km s}^{-1}$ . The magenta spectrum is the same SYN++ model shifted to the inferred velocity of each SLSN.

Table 2
Photospheric Velocities before and after the Maximum for the Nine SLSNe Having Post-maximum Spectra

SLSN	Pre-max Phase (days)	Pre-max  v <sub>phot</sub> (km s <sup>-1</sup> )	Post-max Phase (days)	Post-max $v_{\text{phot}} \atop (\text{km s}^{-1})$	W/ 15bn	Fast/ Slow
SN2010gx	-1	20371	+33	9926	W	F
SN2015bn	-17	9870	+30	8136	15bn	S
SN2016ard	-4	14398	+31	11585	W	S
SN2016eay	-2	20362	+30	9814	W	F
SN2019neq	-4	23000	+29	9972	W	F
LSQ12dlf	-1	15000	+34	7916	15bn	S
PTF09cnd	-14	13200	+28	7593	W	S
PTF10nmn	-1	7871	+28	4307	15bn	S
SSS120810	-1	9870	+30	8136	15bn	S

In contrast, the velocity of PTF09cnd, PTF10nmn, SN 2015bn, SSS120810, SN 2016ard, and LSQ12dlf evolves more slowly: it seems to be nearly constant throughout the observed epochs. It is seen also that these six objects, plotted with different tones of blue in Figure 11, are significantly different from the Fast ones in terms of the photospheric velocity evolution, thus they are called Slow (S) SLSNe-I. This classification is consistent with Inserra et al. (2018), who

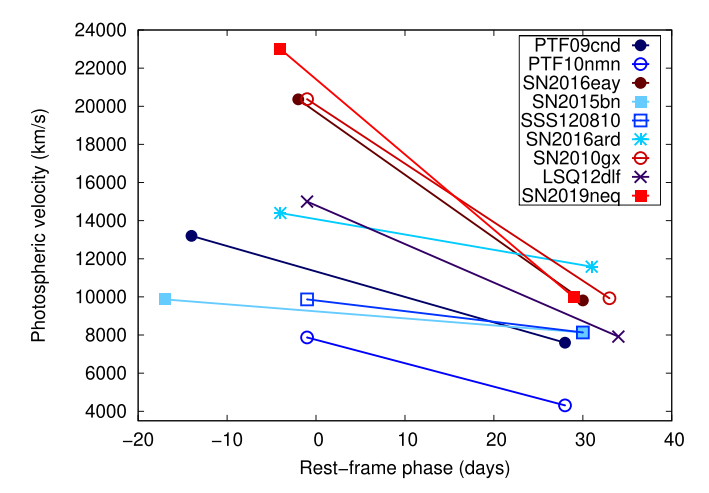


**Figure 11.** Photospheric velocity evolution of the nine SLSNe that possessed both pre-maximum and  ${\sim}30$  days post-maximum spectra. Red symbols denote objects having  $\nu_{\rm phot} {\geqslant} 20{,}000~{\rm km~s}^{-1}$  near maximum (Fast SLSNe-I), while blue colors code the Slow SLSNe-I exhibiting  $\nu_{\rm phot} {\leqslant} 16{,}000~{\rm km~s}^{-1}$  and almost constant velocity evolution.

pointed out that F SLSNe-I tend to have larger velocity gradients and higher  $v_{\text{phot}}$  at maximum than S SLSNe-I.

It is also seen in Figure 11 that the F SLSNe-I are not only swifter in their  $v_{\text{phot}}$  evolution, but their near-maximum

 Table 3

 Results for the Light Curve Rise Times and Ejecta Masses of the Studied SLSNe-I

SLSN	t <sub>obs</sub> [phase] (days)	t <sub>rise</sub> (days)	$M_{ m ej}({f 7}) \ (M_{\odot})$	$M_{ m ej}(8) \ (M_{\odot})$	$M_{ m ej}({ m mean}) \ (M_{\odot})$	$\sigma_{ m sys} \ (M_{\odot})$	$\sigma_{ m rnd} \ (M_{\odot})$	$(\text{km s}^{-1})$	W/15bn	F/S/N
SN2005ap	53436 [-3]	19.64	12.74	6.99	9.86	2.87	3.93	23338	W	F
SN2006oz	54061 [-5]	25.58	13.95	7.66	10.80	3.14	3.40	15064	W	S
SN2010gx	55276 [-1]	25.37	18.55	10.19	14.37	4.18	4.48	20371	W	F
SN2010kd	55528 [-22]	47.68	35.75	19.63	27.69	8.06	5.53	11112	W	S
SN2011kg	55926 [-10]	26.17	11.20	6.15	8.68	2.53	2.75	11562	W	S
SN2015bn	57082 [-17]	90.88	115.34	63.33	89.34	26.01	13.95	9870	15bn	S
SN2016ard	57449 [-4]	25.11	12.85	7.06	9.95	2.90	3.20	14398	W	S
SN2016eay	57528 [-2]	19.25	10.68	5.86	8.27	2.41	3.37	20362	W	F
SN2016els	57599 [-5]	22.35	13.26	7.28	10.27	2.99	3.63	18754	W	N
SN2017faf	57934 [-7]	32.26	26.51	14.56	20.54	5.98	5.15	18000	W	N
SN2018bsz	58259 [-16]	76.17	82.09	45.08	63.58	18.51	10.45	10000	W	S
SN2018hti	58428 [-54]	97.08	197.25	108.31	152.78	44.47	18.07	14790	W	S
SN2018ibb	58453 [-11]	112.24	142.61	78.30	110.45	32.15	19.39	8000	15bn	S
SN2019neq	58722 [-4]	28.21	26.69	14.66	20.68	6.02	5.79	23702	W	F
DES14X3taz	57059 [-29]	44.90	37.13	20.39	28.76	8.37	5.72	13017	W	S
iPTF13ajg	56422 [-5]	47.24	32.07	17.61	24.84	7.23	5.15	10155	W	S
iPTF13ehe	56658 [-14]	82.78	95.69	52.54	74.12	21.58	11.92	9870	15bn	S
LSQ12dlf	56149 [-1]	41.59	36.72	20.16	28.44	8.28	5.84	15000	15bn	S
LSQ14an	56660 [0]	18.23	3.70	2.03	2.87	0.83	1.31	7870	15bn	S
LSQ14bdq	56784 [-11]	46.99	35.35	19.41	27.38	7.97	5.49	11314	W	S
LSQ14mo	56694 [-1]	27.29	10.84	5.95	8.40	2.44	2.61	10284	W	S
PS1-14bj	56744 [-42]	138.81	269.11	147.76	208.44	60.67	29.64	9870	15bn	S
PTF09atu	55034 [-19]	42.09	25.46	13.98	19.72	5.74	4.41	10155	W	S
PTF09cnd	55068 [-14]	54.20	54.86	30.12	42.49	12.37	7.36	13199	W	S
PTF10nmn	55384 [-1]	105.19	123.22	67.66	95.44	27.78	17.16	7870	15bn	S
PTF12dam	56072 [-17]	63.39	68.11	37.40	52.75	15.36	8.60	11978	W	S
PTF12gty	56135 [-4]	48.61	26.74	14.68	20.71	6.03	4.70	8000	15bn	S
SSS120810	56158 [-1]	32.18	14.46	7.94	11.20	3.26	3.07	9869	15bn	S

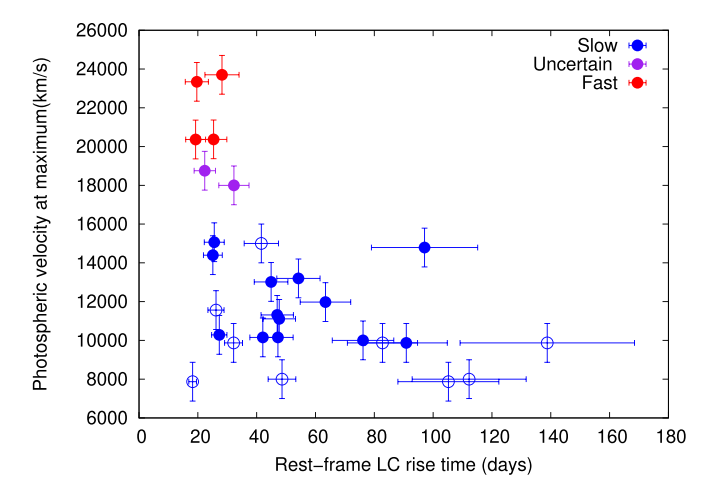


**Figure 12.** Photospheric velocity estimates for the 28 SLSNe in our sample as a function of the light-curve rise time. Filled dots denote Type W objects, while empty circles are the Type 15bn SLSNe-I. Red, and blue colors code the Fast (F), the "uncertain" (N), and the Slow (S) categories, respectively.

 $16,000 \leqslant v_{\rm phot} \leqslant 20,000~{\rm km\,s}^{-1}$  before or near the maximum could not be determined in the absence of  $+30~{\rm day}$  post-maximum data, two objects from our sample, SN 2016els and SN 2017faf, could not be classified into the F or S subgroup unambiguously, as they have a pre-maximum  $v_{\rm phot}$  value of 18,754 and 18,000 km s<sup>-1</sup> respectively. Thus, they are referred as "uncertain" (N) SLSNe-I in Table 3.

In Figure 12, the near-maximum  $v_{\rm phot}$  estimates can be seen as a function of the rest-frame LC rise time for all SLSNe in our sample. The latter was inferred from Equation (5) using the date of explosion ( $t_0$ ) and the moment of the maximum ( $t_{\rm max}$ ) for each object shown in Table 3. Type W SLSNe are plotted with filled symbols, while empty circles denote to the Type 15bn SLSNe. Red, purple, and blue colors code the F, the "uncertain," and the S evolving objects, respectively. It is seen that the SLSNe classified as Fast by their photospheric velocity near maximum are showing short LC rise timescales as well. In contrast, the objects having  $v_{\rm phot} \le 16,000 \, {\rm km \, s^{-1}}$  at maximum exhibit quite diverse LC evolution timescales. It is also apparent that all Type 15bn events (at least those that are analyzed in this paper) belong to the S SLSN-I group.

## 5. Ejecta Mass Estimates

The photospheric velocity estimates presented in Section 4 open the door to derive the ejecta mass of the SLSNe in our sample by applying Equations (7) and (8). To infer the LC rise time ( $t_{rise}$ ) from Equation (5), we used the date of the explosion and the moment of maximum light obtained from the OSC for all objects (see Table 3).

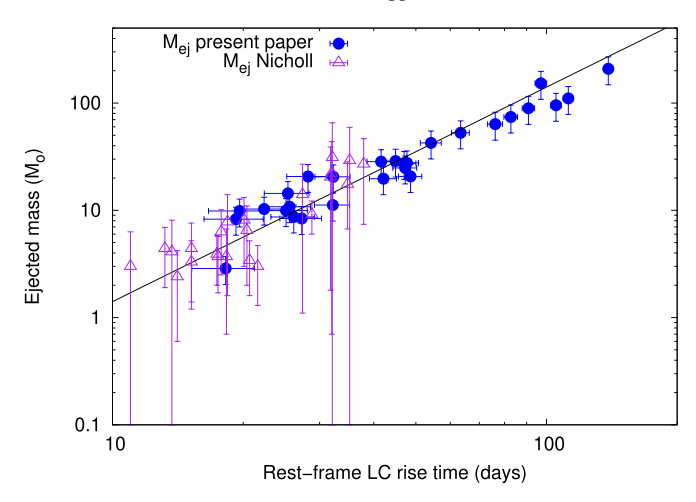


**Figure 13.** Mean ejecta masses from Table 3 (blue dots) as a function of the light-curve (LC) rise time, illustrating that faster LC rise implies smaller ejecta mass. The black line represents the  $M_{\rm ej}({\rm mean}) \sim t_{\rm rise}^2$  relation assuming a uniform expansion velocity of  $10,000~{\rm km~s^{-1}}$  and  $\kappa=0.1~{\rm cm^2~g^{-1}}$  for all objects. The ejecta mass estimates for Type I SLSNe from Nicholl et al. (2015a) are plotted with purple triangles. It is seen that these are systematically lower compared to our mean ejecta mass estimates, but obey the same  $M_{\rm ej} \sim t_{\rm rise}^2$  relation.

Ejecta masses calculated from Equations (7) and (8) can be found in Table 3 among the estimated  $t_{\rm rise}$  and  $v_{\rm phot}$  values. We denote the masses inferred from Equations (7) and (8) as  $M_{\rm ej}(7)$  and  $M_{\rm ej}(8)$ , respectively. We consider their mean, named as  $M_{\rm ej}({\rm mean})$  in Table 3, as our final mass estimate, and the difference between  $M_{\rm ej}(7)$  and  $M_{\rm ej}(8)$  as the systematic uncertainty of our ejecta mass estimate:  $\sigma_{\rm sys} \approx 0.5 \cdot (M_{\rm ej}(7) - M_{\rm ej}(8))$ .

The random errors of  $M_{\rm ej}$ ,  $\sigma_{\rm rnd}$ , due to the uncertainty of the measured  $v_{\rm phot}$  and  $t_{\rm rise}$  (estimated as  $\delta v_{\rm phot} \sim 1000 \, {\rm km \, s}^{-1}$  and  $\delta t_{\rm tise} \sim 3$  days) were also inferred using error propagation. Both  $\sigma_{\rm sys}$  and  $\sigma_{\rm rnd}$  are given in Table 3 for each object.

It is seen that the ejecta masses for the whole sample are in the range from 2.9 ( $\pm 0.8$ ) to 208 ( $\pm 60$ )  $M_{\odot}$ . The mean values are  $\langle M_{\rm ej} \rangle_{\rm ALL} = 42.96 \pm 12.50\,M_{\odot}$  for the 28 events,  $\langle M_{\rm ej} \rangle_{\rm S} = 49.07 \pm 14.80\,M_{\odot}$  for the Slow SLSNe, and  $\langle M_{\rm ej} \rangle_{\rm F} = 14.00 \pm 6.20\,M_{\odot}$  for the Fast and uncertain ones.

Figure 13 displays the inferred ejecta masses (blue points) as a function of the LC rise timescale. It is seen also that the logarithm of the ejecta mass is directly proportional to the logarithm of the LC rise time. This implies that SLSNe having longer rise time tend to have larger ejecta masses compared to the faster evolving objects.

## 5.1. Comparison with Nicholl et al. (2015)

We compared our results to the calculations of Nicholl et al. (2015a), who inferred the ejecta mass of a sample of normal and superluminous supernovae via modeling their bolometric LCs. They utilized an alternative way of using the formula of Arnett (1980) (Equation (8)) by estimating the mean LC timescale as  $t_{\rm m}=0.5\cdot(t_{\rm rise}+t_{\rm dec})$ , where  $t_{\rm dec}$  is the LC decline timescale. They defined  $t_{\rm rise}$ , as the time (t<0) relative to maximum light ( $L_{\rm max}$ ) at which  $L_{\rm griz}=L_{\rm max}/e$ , and  $t_{\rm dec}$  as as the time (t>0) relative to maximum light ( $L_{\rm max}$ ) at which  $L_{\rm griz}=L_{\rm max}/e$ . This is different from both the original definition of Arnett (1980), who used  $t_{\rm m}=\sqrt{2t_dt_h}$  (see Equations (2) and (4)), and from our definition of  $t_{\rm rise}$  (see Equation (5)).

Nicholl et al. (2015a) utilized a different method to estimate the photospheric velocity as well, based on the Fe II  $\lambda 5169$  lines in the spectra, obtaining significantly different values from the  $v_{\rm phot}$  calculations presented in this study. However, as shown in, e.g., Könyves-Tóth et al. (2020), the identification of the Fe II  $\lambda 5169$  line suffers from ambiguity. Thus, we believe that the modeling of the W-shaped O II feature or the whole spectra provide a more reliable method to estimate the photospheric velocities.

In Figure 13, the ejecta mass calculations of Nicholl et al. (2015a) are plotted as a function of their LC rise timescales with purple triangles, in order to compare them to the  $M_{\rm ej}$  calculations of this paper (shown with blue dots). It is seen that the ejecta masses published by Nicholl et al. are systematically smaller than the values calculated in this study, due to the different method of calculating the LC rise timescales, and estimation of the photospheric velocities.

#### 6. Discussion

The main goal of this study was to derive the ejecta masses of all SLSNe having public pre-maximum photometric and spectroscopic observational data in the OSC before 2020. To obtain  $M_{\rm ej}$ , we utilized the formulae of Arnett (1980), summarized in Section 2. Pre- or near-maximum photospheric velocities were crucial to substitute into Equations (7) and (8); thus we developed a method to determine the  $v_{\rm phot}$  of each object in a fast and efficient way.

We found that the W-shaped O II absorption blend, typically present between  $\sim\!3900$  and  $\sim\!4500\,\text{Å}$  in the pre-maximum spectra of Type I SLSNe, is missing from the spectra of nine SLSNe belonging to our sample. These events are found to be spectroscopically similar to SN 2015bn. Therefore, the studied 28 SLSNe were divided into two subtypes by the presence/absence of the W-shaped absorption: the Type W and the Type 15bn groups.

The expansion velocities around maximum light were then estimated for both groups using SYN++ synthetic models and cross-correlation, as described in Section 4. Furthermore, in order to distinguish between fast and slow evolving SLSNe, we repeated this procedure for those events that had public spectra taken around  $\sim$ +30 rest-frame days after maximum.

The fast or slow evolution of a SLSN can be decided from the photospheric velocity gradient between the  $v_{\rm phot}$  measured at the maximum and +30 day phase. Fast SLSNe tend to have larger velocity gradients, while the objects belonging to the Slow group are characterized by much lower velocity gradients or nearly constant photospheric velocities through the observed epochs. This is consistent with the classification scheme of Inserra et al. (2018).

Fast SLSNe-I can also be distinguished from Slow SLSNe-Iby their  $v_{phot}$  at maximum light: the former tend to have  $v_{phot} \geqslant 20,000 \, \mathrm{km \, s}^{-1}$ , while the latter usually have  $v_{phot} \leqslant 16,000 \, \mathrm{km \, s}^{-1}$  instead (see Figure 11).

In some cases, the Fast/Slow classification of a particular object presented in this paper differs from the results of other studies. Five objects out of 28 in our sample (PTF09cnd, PTF10nmn, LSQ14mo, SN 2016ard, and iPTF2016ajg) that were found to be Slow by their  $v_{\rm phot}$  evolution are referred to as Fast SLSNe in e.g., Inserra et al. (2018), Chen et al. (2017b), Blanchard et al. (2018b), and Yu et al. (2017).

The classification of LSQ12dlf is ambiguous as well: in this paper and according to Yu et al. (2017), it seems to be a slow

evolving SLSN, but Inserra et al. (2018) classified it as Fast. The cause of this inconsistency can be found in the different definitions of Fast or Slow evolution: Inserra et al. (2018) found that all objects having  $\nu_{phot} \geqslant 12,000~{\rm km~s^{-1}}$  at maximum belong to the Fast class according to their definition, while we found the threshold to be at  $\nu_{phot} \geqslant 16,000~{\rm km~s^{-1}}$ , near  $\sim\!20,000~{\rm km~s^{-1}}$  in this study. As displayed in Figure 11, SN 2016ard has  $\nu_{phot} \geqslant 12,000~{\rm km~s^{-1}}$  with one of the flattest velocity gradients, while LSQ12dlf shows  $\nu_{phot} \leqslant 16,000~{\rm km~s^{-1}}$  with a medium slope in velocity evolution.

The SLSNe classified into the Fast evolving group by their photospheric velocity measured at maximum belong to the Fast Type I SLSN subgroup by their LC rise times as well. In contrast, objects found to be slowly evolving by  $v_{\rm phot}$  are quite diverse in  $t_{\rm rise}$ , ranging between a few weeks and  $\sim 150$  days (see Figure 12).

All SN 2015bn-like SLSNe are classified to the Slow group by their  $v_{\text{phot}}$ , while among the Type W events both Fast and Slow objects are represented.

The mean and range of the estimated ejecta masses for the 28 SLSNe in our sample,  $\langle M_{\rm ej} \rangle_{\rm ALL} = 42.96 \pm 12.50\,M_{\odot}$  between 3 and 208  $M_{\odot}$ , are significantly higher than the  $M_{\rm ej}$  estimates presented by Nicholl et al. (2015a) ( $\langle M_{\rm ej} \rangle \sim 10\,M_{\odot}$ , between 3 and 30  $M_{\odot}$  for their sample). The difference is due to the different method of calculating photospheric velocities and LC timescales.

It is also interesting that the mean mass of the Fast events (including the uncertain ones) in our sample  $(\langle M_{\rm ej} \rangle_{\rm F} = 14.00 \pm 6.20\,M_{\odot})$  is significantly lower than that of the Slow events  $(\langle M_{\rm ej} \rangle_{\rm S} = 49.07 \pm 14.80\,M_{\odot})$ . At first glance this suggests that the physical cause of the Fast/Slow dichotomy could be related to the amount of the ejected envelope. However, as the sample is still very poor (only 28 objects), more data are urgently needed to be able to draw more reliable conclusion.

# 7. Summary

We have presented photospheric velocity estimates and ejecta mass calculations of a sample containing 28 Type I SLSNe having publicly available photometric and spectroscopic data in the OSC (Guillochon et al. 2017).

We utilized the formulae of the radiation–diffusion model of Arnett (1980) to estimate the ejecta masses. The LC rise time and the photospheric velocity before or near the luminosity maximum was necessary to obtain the  $M_{\rm ej}$  values.

The photospheric velocities of the sample SLSNe were estimated utilizing a method combining spectrum modeling with cross-correlation, similar to Takáts & Vinkó (2012). It was found that the W-shaped O II absorption blend, typically present in the pre-maximum spectra of SLSNe-I, is missing from the spectra of several objects that otherwise have very similar features to SN 2015bn. Thus, two groups of the sample SLSNe were created (called Type W and Type 15bn), and their  $v_{\rm phot}$  values obtained using different SYN++ model spectra as templates in the cross-correlation.

Post-maximum  $v_{\rm phot}$  values of nine SLSNe with available spectra were also estimated in a similar way in order to to classify these events into the Fast or the Slow SLSN subtypes by calculating the velocity gradients between the maximum, and +30 rest-frame days. Fast SLSNe showed considerably higher velocity gradients than Slow ones, in good agreement with Inserra et al. (2018).

These calculations also confirmed that Fast SLSNe generally show higher velocities close to maximum than Slow events. This allowed us to classify other SLSNe in our sample that did not have public spectra around +30 days. Thus, we considered the SLSNe having  $\nu_{\rm phot} \geqslant 20,000~{\rm km~s^{-1}}$  near maximum as Fast, and the events with  $\nu_{\rm phot} \leqslant 16,000~{\rm km~s^{-1}}$  as Slow. Among the studied SLSNe, the Fast evolving objects defined

Among the studied SLSNe, the Fast evolving objects defined by the photospheric velocities were revealed to show a rapidly evolving LC with a short LC rise time as well. In contrast, Slow evolving events having lower  $v_{\rm phot}$  had more diverse LC rise timescales, ranging from a few weeks to  $\sim 150$  days. It was also found that all Type 15bn events belonged to the Slow evolving SLSN-I subgroup defined by  $v_{\rm phot}$ , while Type W objects were represented in both the Fast and Slow groups.

Ejecta mass calculations of the SLSNe in our sample were carried our using Equations (7) and (8), resulting in masses within a range 2.9 ( $\pm 0.8$ )–208 ( $\pm 61$ )  $M_{\odot}$ , having a mean of  $\langle M_{\rm ej} \rangle = 42.96 \pm 12.50\,M_{\odot}$ . This is significantly larger than the  $\langle M_{\rm ej} \rangle$  calculated by Nicholl et al. (2015a), who obtained  $\langle M_{\rm ej} \rangle \sim 10\,M_{\odot}$  between 3 and 30  $M_{\odot}$  for a different sample of SLSNe-I using different methods to estimate the photospheric velocities and LC evolution timescales.

The mean ejecta mass of Slow SLSNe in our sample  $(\sim 49 \pm 15~M_{\odot})$  seems to be higher than that of the Fast ones  $(\sim 14 \pm 6\,M_{\odot})$ , suggesting a physical link between the Fast/Slow dichotomy and the ejecta mass. However, since it is based on only 28 (24 Slow and four Fast) objects, more data are required for a more reliable conclusion.

Our ejecta mass estimates further strengthen the longstanding concept that SLSNe probably originate from a range of moderately massive to very massive progenitors, and their (still uncertain) explosion mechanism is able to eject large amounts of their envelope mass.

Our study is supported by the project "Transient Astrophysical Objects" GINOP 2.3.2-15-2016-00033 of the National Research, Development and Innovation Office (NKFIH), Hungary, funded by the European Union. We thank the anonymous referee for the thorough report and useful comments that led to significant improvement of this paper.

## **Appendix**

Table A1 summarizes the selection process of out sample. Here we describe in detail the reason for removing 13 SLSNe-I having pre-maximum spectra.

- 1. The pre-maximum spectra of SN 2019szu, SCP-06F6, and OGLE15qz were so noisy that spectral features could not be identified at all.
- 2. DES15E2mlf, SNLS-06D4eu, and SNLS-07D2bv were observed only in the UV bands up to 3000 Å.
- The spectra taken of SN 2010md, PTF10vqv, SN 2016aj, and SN 2010uhf did not contain typical SLSN-I spectral features, or the W-like absorption between 3900 and 4500 Å, which is usually present in the pre-maximum spectra of SLSNe-I.
- The selected spectrum of SN 2007bi was actually taken after the maximum.
- 5. SN 2015L, the most luminous "SLSN" ever seen, is presumably a tidal disruption event (e.g., Leloudas et al. 2016; Margutti et al. 2017; Coughlin & Armitage 2018). If we assume it to be an SLSN, it interacts so robustly that

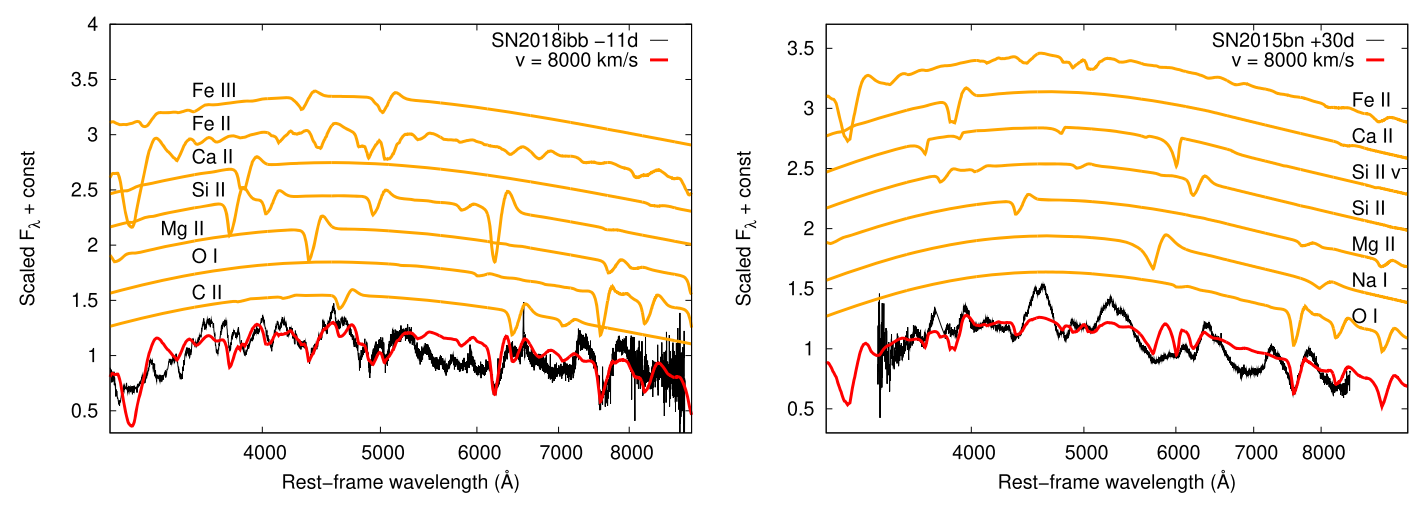


**Figure A1.** Left panel: -11 day rest-frame phase spectrum of SN 2018ibb (black), belonging to the Type 15bn group of SLSNe-I together with its best-fit model obtained in SYN++ (red). Single-ion contributions to the overall model spectrum are plotted with orange, shifted vertically to guide the eye. Right panel: same as left for the +30 day phase spectrum of SN 2015bn.

Table A1
SLSNe Removed from Our Sample

Reason for Exclusion [Number]	SLSN
SLSNe-II [18]	SN2006gy, SN1000+0216, SN2008am, SN2008es, CSS121015:004244+132827, PTF12mkp, SN2013hx, PS15br, LSQ15abl, SN2016aps, SN2016ezh, SN2016jhm, SN2016jhn, SN2017bcc, SN2017egm, SN2018jkq, SN2019cmv, SN2019meh
Without pre-maximum spectra [39]	SN2213-1745, SDSS-II SN 2538, SDSS-II SN17789, SN2009cb, SN2009jh, PTF10bfz, PTF10bfp, PS1-10pm, PS1-10ky, PS1-11tt, PS1-10ahf, SN2010hy, PS1-10awh, PTF10aagc, PS1-10bzj, PS1-11ap, SN2011ke, PS1-11afv, PTF11hrq, SN2011kl, SN2011kf, SN2012il, PTF12mxx, SN2013dg, SN2013hy, CSS130912:025702-001844, PS15cjz, OGLE15sd, PS16yj, iPTF16bad, DES16C2nm, AT2016jho, SN2017jan, DES17C3gyp, SN2018bgv, SN2018gkz, SN2018lfd, SN2019meh, SN2019szu
Problem with spectra [13]	SN 2019stu, SN2019steil, SN2019szu SN 2019szu, SCP-06F6, OGLE15qz, DES15E2mlf, SNLS-06D4eu, SNLS-07D2bv, SN 2010md, PTF10vqv, SN 2016aj, SN 2010uhf, SN 2007bi, SN 2015L, SN 2017gir

		Type W	SLSNe		
		Global pa	rameters		
$a_0$	$\frac{v_{\rm phot}}{({\rm km~s}^{-1})}$	$T_{\rm phot}$ (10 <sup>3</sup> K)			
1.0	10,000–30,000	15,000			
		Local par	rameters		
Element	$\log au$	$v_{\rm min} \ (10^3 \ {\rm km \ s^{-1}})$	$v_{\rm max} \ (10^3 {\rm \ km \ s^{-1}})$	$\frac{aux}{(10^3 \text{ km s}^{-1})}$	$T_{\rm exc} \ (10^3 \ {\rm K})$
O II	-2.0	$v_{ m phot}$	50.0	2.0	15.0
		Type 15bi	1 SLSNe		
		Global pa	rameters		
$a_0$	$v_{\rm phot} ({\rm km \ s}^{-1})$	$T_{\rm phot}$ (10 <sup>3</sup> K)			
0.7	8000-30,000	11,000			
		Local par	rameters		
Element	$\log au$	$v_{\rm min} \ (10^3 \ {\rm km \ s^{-1}})$	$v_{\rm max} \ (10^3 {\rm \ km \ s^{-1}})$	$\frac{aux}{(10^3 \text{ km s}^{-1})}$	$T_{\rm exc}$ $(10^3 \text{ K})$
Сп	-1.4	$v_{ m phot}$	50.0	1.0	10.0
OI	0.3	$v_{ m phot}$	50.0	1.0	10.0
Mg II	0.0	$v_{ m phot}$	50.0	1.0	10.0
Si II	0.5	$v_{ m phot}$	50.0	1.0	10.0

Table A2 (Continued)

		(Contin						
Type W SLSNe								
Ca II	0.0	$v_{ m phot}$	50.0	1.0	10.0			
Fe II	0.0	$v_{ m phot}$	50.0	1.0	12.0			
Fe III	-0.5	$v_{ m phot}$	50.0	1.0	10.0			
		SLSNe after	maximum					
		Global pa	rameters					
$a_0$	$\frac{v_{\rm phot}}{({\rm km~s}^{-1})}$	$T_{\rm phot}$ (10 <sup>3</sup> K)						
0.7	5000-15,000	9000						
		Local par	rameters					
Element	$\log  au$	$v_{\rm min} \ (10^3 \ {\rm km \ s}^{-1})$	$v_{\rm max} \ (10^3 {\rm \ km \ s}^{-1})$	$\frac{aux}{(10^3 \text{ km s}^{-1})}$	$T_{\rm exc}$ (10 <sup>3</sup> K)			
01	0.1	$v_{\rm phot}$	50.0	1.0	10.0			
Na I	-0.5	$v_{\rm phot}$	50.0	4.0	10.0			
Mg II	-0.5	$v_{ m phot}$	50.0	1.0	10.0			
Si II	-0.3	$v_{ m phot}$	50.0	1.0	10.0			
Si II v	0.7	17.0	50.0	3.0	10.0			
Ca II	0.0	$v_{ m phot}$	50.0	1.0	10.0			
Fe II	-0.5	$v_{ m phot}$	50.0	1.0	12.0			

the photosphere is not even visible, thus it is impossible to estimate the photospheric velocity in the maximum.

SN 2017gir had a spectrum more similar to a Type II SLSN.

In Figure A1, the SYN++ modeling of the -11 day phase spectrum of SN 2018ibb (Type 15bn; left panel) and the +30 day phase spectrum of SN 2015bn (right panel) are plotted.

Table A2 summarizes the global and local SYN++ parameters obtained for Type W, Type 15bn, and post-maximum SLSN spectra.

#### ORCID iDs

Réka Könyves-Tóth https://orcid.org/0000-0002-8770-6764

József Vinkó https://orcid.org/0000-0001-8764-7832

## References

```
Anderson, J. P., Pessi, P. J., Dessart, L., et al. 2018, A&A, 620, A67
Angus, C. R., Levan, A. J., Perley, D. A., et al. 2016, MNRAS, 458, 84
Angus, C. R., Smith, M., Sullivan, M., et al. 2019, MNRAS, 487, 2215
Arabsalmani, M., Roychowdhury, S., Renaud, F., et al. 2019, ApJ, 882, 31
Arnett, W. D. 1980, ApJ, 237, 541
Arnett, W. D. 1982, ApJ, 253, 785
Arnett, W. D., & Fu, A. 1989, ApJ, 340, 396
Bassett, B., Becker, A., Brewington, H., et al. 2006, CBET, 762, 1
Benetti, S., Nicholl, M., Cappellaro, E., et al. 2014, MNRAS, 441, 289
Benitez, S., Polshaw, J., Inserra, C., et al. 2014, ATel, 6118, 1
Blanchard, P., Nicholl, M., Chornock, R., et al. 2018a, ATel, 11790, 1
Blanchard, P. K., Nicholl, M., Berger, E., et al. 2018b, ApJ, 865, 9
Bose, S., Dong, S., Pastorello, A., et al. 2018, ApJ, 853, 57
Branch, D., & Wheeler, J. C. 2017, Supernova Explosions: Astronomy and
   Astrophysics Library (Berlin: Springer)
Brown, P. J., Breeveld, A. A., Holland, S., et al. 2014, Ap&SS, 354, 89
Burke, J., Hiramatsu, D., Arcavi, I., et al. 2018, Transient Name Server
   Classification Report, 2018-1719
Castander, F. J., Casas, R., Garcia-Alvarez, D., et al. 2015, ATel, 7190, 1
Chandra, P., Ofek, E. O., Frail, D. A., et al. 2009, ATel, 2241, 1
Chatzopoulos, E., Wheeler, J. C., & Vinko, J. 2012, ApJ, 746, 121
Chatzopoulos, E., Wheeler, J. C., Vinko, J., et al. 2013, ApJ, 773, 76
```

```
Chen, T.-W., Nicholl, M., Smartt, S. J., et al. 2017a, A&A, 602, A9
Chen, T.-W., Schady, P., Xiao, L., et al. 2017b, ApJL, 849, L4
Chen, T.-W., Smartt, S. J., Bresolin, F., et al. 2013, ApJL, 763, L28
Chen, T.-W., Smartt, S. J., Yates, R. M., et al. 2017c, MNRAS, 470, 3566
Chornock, R., Bhirombhakdi, K., Katebi, R., et al. 2016, ATel, 8790, 1
Coughlin, E. R., & Armitage, P. J. 2018, MNRAS, 474, 3857
De Cia, A., Gal-Yam, A., Rubin, A., et al. 2018, ApJ, 860, 100
Dessart, L. 2019, A&A, 621, A141
Drake, A. J., Djorgovski, S. G., Mahabal, A., et al. 2009, ApJ, 696, 870
Fraser, M., Reynolds, T., Mattila, S., et al. 2016, Transient Name Server
   Classification Report, 2016-521
Gal-Yam, A. 2009, GALEX Proposal, 35
Gal-Yam, A. 2012, Sci, 337, 927
Gal-Yam, A. 2019a, ARA&A, 57, 305
Gal-Yam, A. 2019b, ApJ, 882, 102
Green, D. W. E. 2006, CBET, 762, 7
Guillochon, J., Parrent, J., Kelley, L. Z., et al. 2017, ApJ, 835, 64
Hatsukade, B., Morokuma-Matsui, K., Hayashi, M., et al. 2020, PASJ, 72, 6
Hatsukade, B., Tominaga, N., Hayashi, M., et al. 2018, ApJ, 857, 72
Hiramatsu, D., Arcavi, I., Burke, J., et al. 2018, Transient Name Server
   Classification Report, 2018-679
Inserra, C. 2019, NatAs, 3, 697
Inserra, C., Nicholl, M., Chen, T.-W., et al. 2017, MNRAS, 468, 4642
Inserra, C., Prajs, S., Gutierrez, C. P., et al. 2018, ApJ, 854, 175
Inserra, C., Smartt, S. J., Jerkstrand, A., et al. 2013, ApJ, 770, 128
Izzo, L., Thöne, C. C., García-Benito, R., et al. 2018, A&A, 610, A11
Japelj, J., Vergani, S. D., Salvaterra, R., et al. 2016, A&A, 593, A115
Kangas, T., Blagorodnova, N., Mattila, S., et al. 2017, MNRAS, 469, 1246
Kangas, T., Elias-Rosa, N., Lundqvist, P., et al. 2016, ATel, 9071, 1
Kasen, D., Woosley, S. E., & Heger, A. 2011, ApJ, 734, 102
Khatami, D. K., & Kasen, D. N. 2019, ApJ, 878, 56
Kilpatrick, C. 2017, Transient Name Server Classification Report, 2017-719
Könyves-Tóth, R., Thomas, B. P., Vinkó, J., et al. 2020, ApJ, 900, 73
Kumar, A., Pandey, S. B., Konyves-Toth, R., et al. 2020, ApJ, 892, 28
Le Guillou, L., Mitra, A., Baumont, S., et al. 2015, ATel, 7102, 1
Leget, P.-F., Le Guillou, L., Fleury, M., et al. 2014, ATel, 5718, 1
Leloudas, G., Chatzopoulos, E., Dilday, B., et al. 2012, A&A, 541, A129
Leloudas, G., Ergon, M., Taddia, F., et al. 2014, ATel, 5839, 1
Leloudas, G., Fraser, M., Stone, N. C., et al. 2016, NatAs, 1, 0002
Leloudas, G., Schulze, S., Krühler, T., et al. 2015, MNRAS, 449, 917
Lennarz, D., Altmann, D., & Wiebusch, C. 2012, A&A, 538, A120
Levan, A. J., Read, A. M., Metzger, B. D., et al. 2013, ApJ, 771, 136
Liu, Y.-Q., Modjaz, M., & Bianco, F. B. 2017, ApJ, 845, 85
Lunnan, R., Chornock, R., Berger, E., et al. 2013, ApJ, 771, 97
Lunnan, R., Chornock, R., Berger, E., et al. 2014, ApJ, 787, 138
Lunnan, R., Chornock, R., Berger, E., et al. 2016, ApJ, 831, 144
```

```
Lunnan, R., Chornock, R., Berger, E., et al. 2018, ApJ, 852, 81
Maeda, K., Tanaka, M., Nomoto, K., et al. 2007, ApJ, 666, 1069
Margutti, R., Metzger, B. D., Chornock, R., et al. 2017, ApJ, 836, 25
Mazzali, P. A., Sullivan, M., Pian, E., et al. 2016, MNRAS, 458, 3455
Modjaz, M., Kirshner, R., Challis, P., et al. 2005, IAUC, 8492, 3
Nagy, A. P. 2018, ApJ, 862, 143
Nagy, A. P., Ordasi, A., Vinkó, J., et al. 2014, A&A, 571, A77
Nagy, A. P., & Vinkó, J. 2016, A&A, 589, A53
Neill, J. D., Sullivan, M., Gal-Yam, A., et al. 2011, ApJ, 727, 15
Nicholl, M., Berger, E., Margutti, R., et al. 2016a, ApJL, 828, L18
Nicholl, M., Berger, E., Margutti, R., et al. 2017a, ApJL, 835, L8
Nicholl, M., Berger, E., Margutti, R., et al. 2017b, ApJL, 845, L8
Nicholl, M., Berger, E., Smartt, S. J., et al. 2016b, ApJ, 826, 39
Nicholl, M., Guillochon, J., & Berger, E. 2017c, ApJ, 850, 55
Nicholl, M., Smartt, S. J., Jerkstrand, A., et al. 2013, Natur, 502, 346
Nicholl, M., Smartt, S. J., Jerkstrand, A., et al. 2014, MNRAS, 444, 2096
Nicholl, M., Smartt, S. J., Jerkstrand, A., et al. 2015a, MNRAS, 452, 3869
Nicholl, M., Smartt, S. J., Jerkstrand, A., et al. 2015b, ApJL, 807, L18
Nordin, J., Brinnel, V., Giomi, M., et al. 2019, Transient Name Server
   Discovery Report, 2019-1472
Ofek, E. O., Fox, D., Cenko, S. B., et al. 2013, ApJ, 763, 42
Pastorello, A., Benetti, S., Cappellaro, E., et al. 2017, ATel, 10554, 1
Pastorello, A., Smartt, S. J., Botticella, M. T., et al. 2010a, CBET, 2413, 1
Pastorello, A., Smartt, S. J., Botticella, M. T., et al. 2010b, ApJL, 724, L16
Perley, D. A. 2019, Transient Name Server Classification Report, 2019-1646
Perley, D. A., Quimby, R. M., Yan, L., et al. 2016, ApJ, 830, 13
Perley, D. A., Yan, L., Gal-Yam, A., et al. 2019, TNSAN, 79, 1
Pinto, P. A., & Eastman, R. G. 2000a, ApJ, 530, 744
Pinto, P. A., & Eastman, R. G. 2000b, ApJ, 530, 757
Piro, A. L., & Nakar, E. 2014, ApJ, 784, 85
```

```
Popov, D. V. 1993, ApJ, 414, 712
Puckett, T., Crowley, T., Quimby, R., et al. 2005, IAUC, 8492, 1
Pursiainen, M., Castro-Segura, N., Smith, M., et al. 2018, Transient Name
  Server Classification Report, 2018-2184
Quimby, R. M., Aldering, G., Wheeler, J. C., et al. 2007, ApJL, 668, L99
Quimby, R. M., Arcavi, I., Sternberg, A., et al. 2012, ATel, 4121, 1
Quimby, R. M., De Cia, A., Gal-Yam, A., et al. 2018, ApJ, 855, 2
Quimby, R. M., Gal-Yam, A., Arcavi, I., et al. 2013, CBET, 3464, 1
Quimby, M., Kulkarni, S. R., Kasliwal, M. M., et al. 2011, Natur, 474,
Sako, M., Bassett, B., Becker, A. C., et al. 2018, PASP, 130, 064002
Schlafly, E. F., & Finkbeiner, D. P. 2011, ApJ, 737, 103
Schulze, S., Krühler, T., Leloudas, G., et al. 2018, MNRAS, 473, 1258
Shivvers, I., Filippenko, A. V., Silverman, J. M., et al. 2019, MNRAS,
  482, 1545
Smartt, S. J., Inserra, C., Fraser, M., et al. 2012, ATel, 4299, 1
Smartt, S. J., Valenti, S., Fraser, M., et al. 2015, A&A, 579, A40
Smith, M., Sullivan, M., D'Andrea, C. B., et al. 2016, ApJL, 818, L8
Smith, N., Li, W., Foley, R. J., et al. 2007, ApJ, 666, 1116
Takáts, K., & Vinkó, J. 2012, MNRAS, 419, 2783
Thomas, R. C., Nugent, P. E., & Meza, J. C. 2011, PASP, 123, 237
Tonry, J., Denneau, L., Heinze, A., et al. 2018, Transient Name Server
  Discovery Report, 2018-1680
Valenti, S., Benetti, S., Cappellaro, E., et al. 2008, MNRAS, 383, 1485
Vreeswijk, P. M., Savaglio, S., Gal-Yam, A., et al. 2014, ApJ, 797, 24
Wright, D., Cellier-Holzem, F., Inserra, C., et al. 2012, ATel, 4313, 1
Yan, L., Perley, D. A., De Cia, A., et al. 2018, ApJ, 858, 91
Yan, L., Quimby, R., Ofek, E., et al. 2015, ApJ, 814, 108
Yaron, O., & Gal-Yam, A. 2012, PASP, 124, 668
Yu, Y.-W., Zhu, J.-P., Li, S.-Z., et al. 2017, ApJ, 840, 12
```